

CAMS Service Evolution



D5.5 Intercomparison of satellite-derived CO₂, CH₄ and NO_x emissions

Due date of deliverable	Dec 2024
Submission date	Jan 2025
File Name	CAMEO-D5-5-V1.0
Work Package /Task	WP5 Task 5.4
Organisation Responsible of Deliverable	LSCE, KNMI
Author name(s)	Philippe Ciais, Kushal Tibrewal, Qinren Shi, Ronald van der A, Jieying Ding, Nicolas Boussez
Revision number	1
Status	Issued
Dissemination Level	Public



Funded by the
European Union

The CAMEO project (grant agreement No 101082125) is funded by the European Union.

Views and opinions expressed are however those of the author(s) only and do not necessarily reflect those of the European Union or the Commission. Neither the European Union nor the granting authority can be held responsible for them.

1 Executive Summary

This deliverable presents the evaluation of satellite derived CAMEO IFS inversions of surface fluxes of CO₂ anthropogenic emissions, CH₄ emissions from the fossil fuel sector and NO_x emissions against independent data streams. For CO₂, we included point scale inversions of XCO₂ (column averaged CO₂ mixing ratio) excess in plumes from cities and power plants crossed on orbit by OCO₂ and OCO-2 spaceborne sensors. For CH₄, we included point scale inversions of CH₄ emissions from ultra-large emitting events traced from TROPOMI images (typically leak events with a release rate higher than 20 tCH₄ per hour which last between a few hours and a few days, with exception of rare persistent events), basin scale inversions of emissions over extractive regions obtained with a high resolution inversion of satellite images from TROPOMI, and large scale fossil CH₄ emissions diagnosed by global inversions used in the Global Carbon Project CH₄ budget analysis. Those global inversions are based either on GOSAT satellite soundings or on ground-based station time series (including the most recent update of the global methane budget up to the year 2020). We also compared CH₄ inversion results with different bottom-up inventories representing gridded CH₄ emissions from activity data combined with emission factors. For NO_x, we evaluated the IFS inversions with the DECSO inverse model of NO_x emissions, with a focus on point sources and cities, and with various NO_x inventories. The results for CO₂ point sources show large differences between the CAMEO IFS inversion and local inversions from OCO-2 and OCO-3 satellites sparse plumes sampling. The results for the CH₄ inversion shows a fair comparison with regional budgets of other global inversions, but does not seem to detect much sporadic point leaks emissions. The inversion fluxes for CH₄ over large regions show spikes perhaps related to the short assimilation window used. For NO_x, the magnitude of CAMEO IFS emissions for industrial sources are comparable to other inventories, but its city emissions were usually lower and rural emissions were higher. The resolution of the CAMEO emissions (80 km) was visibly lower in the maps than other inventories (10-20 km). However, the analysis increments of CAMEO showed an even lower resolution, maybe because of the long correlation length of the spatial error in the IFS system. This might also be the explanation that some strong point sources remain persistent in the CAMEO emissions but are unknown in other inventories.

Table of Contents

1	Executive Summary	2
2	Introduction	4
2.1	Background.....	4
2.2	Scope of this deliverable	4
2.2.1	Objectives of this deliverables.....	4
2.2.2	Work performed in this deliverable.....	4
2.3	Evaluation of CO ₂ inversion results	5
2.3.1	Point & area sources emissions retrieved from OCO-2 and OCO-3.....	5
2.3.2	Global IFS CO ₂ , CH ₄ and NO _x inversion.....	6
2.3.3	Point and area sources emissions compared with IFS CO ₂ inversion	6
2.4	Evaluation of CH ₄ inversions.....	8
2.4.1	Global inversions models.....	8
2.4.2	CAMEO data collected and processed for inversions evaluation.....	8
2.4.3	Results of inversions comparisons.....	16
2.5	Evaluation of NO _x inversions	24
2.5.1	Inversion algorithms of NO _x	24
2.5.2	Emission data for evaluation	26
2.5.3	Results for NO _x emissions.....	27
2.6	Conclusions	37
2.7	Deviations and countermeasures.....	37
2.8	CAMEO Project Partners:	38
2.9	References	39
	Document History	46

2 Introduction

2.1 Background

Monitoring the composition of the atmosphere is a key objective of the European Union's flagship Space programme Copernicus, with the Copernicus Atmosphere Monitoring Service (CAMS) providing free and continuous data and information on atmospheric composition. The CAMS Service Evolution (CAMEO) project aims to enhance the quality and efficiency of the CAMS service and help CAMS to better respond to policy needs such as air pollution and greenhouse gas monitoring, the fulfilment of sustainable development goals, and sustainable and clean energy. CAMEO will help prepare CAMS for the uptake of forthcoming satellite data, including Sentinel-4, -5 and 3MI, and advance the aerosol and trace gas data assimilation methods and inversion capacity of the global and regional CAMS production systems. CAMEO will develop methods to provide uncertainty information about CAMS products, in particular for emissions, policy, solar radiation and deposition products in response to prominent requests from current CAMS users. CAMEO will contribute to the medium- to long-term evolution of the CAMS production systems and products.

The transfer of developments from CAMEO into subsequent improvements of CAMS operational service elements is a main driver for the project and is the main pathway to impact for CAMEO. The CAMEO consortium, led by ECMWF, the entity entrusted to operate CAMS, includes several CAMS partners thus allowing CAMEO developments to be carried out directly within the CAMS production systems and facilitating the transition of CAMEO results to future upgrades of the CAMS service. This will maximise the impact and outcomes of CAMEO as it can make full use of the existing CAMS infrastructure for data sharing, data delivery and communication, thus supporting policymakers, business and citizens with enhanced atmospheric environmental information.

In the CAMEO project, a central component is the IFS inversion developed in the Copernicus Atmosphere Monitoring Service (CAMS) employs a four-dimensional variational (4D-Var) data assimilation system within the European Centre for Medium-Range Weather Forecasts (ECMWF) Integrated Forecasting System (IFS). This system integrates atmospheric composition observations with model forecasts to produce accurate analyses and forecasts of atmospheric constituents such as aerosols and trace gases.

2.2 Scope of this deliverable

2.2.1 Objectives of this deliverables

The IFS inversion was developed in the recent years and produced results in 2024. The results of the inversion have not yet been evaluated. This deliverable has the objective to present the evaluation data used to evaluate the IFS inversion system for surface fluxes of CO₂, CH₄ and NO_x, and to present the first results of the inversion evaluation. The IFS inversion results have been provided by ECMWF on July 17, 2024 and the evaluation is presented based on work performed during the last four months before submission of the deliverable.

2.2.2 Work performed in this deliverable

Following the Description of Work of WP5 of the CAMEO Project “*WP5 will prepare a framework for the Evaluation and quality control (EQC) of the global CAMS observation-based emissions estimates developed as part of the CAMS core services. Emissions of CO₂, CH₄ and NO_x derived from the CAMS global inverse system will be compared against estimates obtained from state-of-the-art inversion systems with an improved spatial resolution. Emissions derived through inverse modelling will also be used to assess the consistency with the current CAMS emission products in terms of country reported total emissions and their spatial and temporal distributions*”. The goal of Task 5.4 in WP4 is to perform an evaluation and quality control (EQC) framework for the global CAMS observation-based emissions estimates. This Deliverable presents the first results of this evaluation.

2.3 Evaluation of CO₂ inversion results

For CO₂, we focus on the collection and processing of independent validation data. Since emission inventories are prescribed as a prior of inversions for fossil fuel and cement CO₂ emissions, they cannot be used for evaluation. Therefore, we collected independent estimates of CO₂ emissions that can be retrieved directly from Gaussian plume inversion models applied to selected suitable orbits of the two Orbiting Carbon Observatories (OCO) OCO-2 and OCO-3 to invert emissions from column CO₂.

2.3.1 Point & area sources emissions retrieved from OCO-2 and OCO-3

Using the multiyear archive of the two Orbiting Carbon Observatories (OCO) of NASA from 2015 to 2022, we have retrieved the emissions of large fossil fuel CO₂ emitters over the globe with a simple plume cross-sectional inversion approach. We have compared our results with a global gridded and hourly inventory from EDGARV6, and the corresponding OCO emission retrievals explain more than one third of the inventory variance at the corresponding cells and hours ([Chevallier et al.\(2022\)](#)). We have binned the data at diverse time scales from yearly (with OCO-2) to the average morning and afternoon (with OCO-3).

Our approach to retrieve the CO₂ emissions from the anthropogenic plume transects seen by the OCO instruments closely follows the detailed description made in [Zheng et al. \(2020\)](#) and [Chevallier et al. \(2020\)](#). We therefore briefly summarize it and explain the few refinements that we have brought to it since then. We process data from both instruments in exactly the same way.

Each OCO orbit is analysed with a 200 km moving window successively centred on each of the validated retrieval. If a retrieval value stands out of the variability of the retrievals in the window, the procedure attempts to fit a function that represents a bell curve on top of a linear background, on the soundings located over the dominant surface type in the window. For the Snapshot Area Mapping observation mode of OCO-3 targeted at cities and intense emission areas, we exclude the retrievals from the fit that are not in the same scan line, in order to stay within a cross-sectional vision. The soundings are represented by their XCO₂ retrievals and by their position along the satellite track: their across-track position is ignored as the satellite narrow swath is used only to dampen retrieval noise. The restriction to the soundings of the dominant surface type (either land or ocean) mainly removes the enhancements which are partially on inland waters that we suspect of inducing artificial discontinuities in the retrievals. The adjustable parameters are the standard deviation σ_{gauss} and the height of the Gaussian, and the slope and offset of the line defining the background. The center of the peak is positioned in the middle of the 200 km moving window and is not adjusted. The choice of the Gaussian form is linked to its neutrality (in the sense of the principle of maximum entropy) rather than to a hypothesis on the exact shape of the plume. In particular, a visual inspection of the orbits reveals that many XCO₂ enhancements take the form of Gaussian mixtures that can still be well adjusted by a single Gaussian: these ones are retained by the automatic process.

The quality of the fit is evaluated by the following criteria (numerical values given only when they differ from [Chevallier et al., 2020](#)): (i) its r^2 (it has to be larger than 0.7²), (ii) the density of the retrievals within 1 sigma of the Gaussian center, and between 2 and 3 sigma of it, (iii) the value of the Gaussian standard deviation σ_{gauss} (it must be between 2 and 30 km, except for the 80x80 km² SAM observation mode of OCO-3, for which the maximum acceptable σ_{gauss} is reduced to 20 km), (iv) the value of the Gaussian height relative to the retrieval variability in the window. A validated fit is interpreted as reflecting a situation where the orbit is crossing of a CO₂ plume from an emitting area or point source. If several validated fitting functions, centered on different retrievals, overlap, only the one with the largest r^2 is kept. Such an overlap can happen for instance between estimates made from different scan lines of a SAM.

CAMEO

The area under the Gaussian gives the XCO₂ line density, which is multiplied with the wind speed in the direction normal to the OCO track to retrieve the corresponding emission under the assumption of a steady wind. The wind speed is taken from the fifth generation of ECMWF atmospheric reanalyses of the global climate (ERA5, [Hersbach et al., 2020](#)) in the model ninth level from the surface, that corresponds to a geometric altitude of about 250 m (after [Brunner et al., 2019](#)). The cases with retrieved emissions less than 0.5 ktCO₂ h⁻¹ are judged as unreliable and are left out. This detection threshold is comparable to the one found by [Lespinas et al. \(2020\)](#).

This set of emission retrievals is then filtered to keep only the fresh plumes, defined here as plumes which are mostly less than 3 hours old, because older ones have a more complex transport history. In [Chevallier et al. \(2020\)](#), we used a loose criterion based on satellite retrievals of the nitrogen dioxide column. Here we use a stricter criterion, in which only OCO-observed plume transects that are either downwind of, or less than 30 km from, a 0.1°×0.1° cell of EDGAR where an emission of at least 1.0 ktCO₂ h⁻¹ is reported (see Section 2d below for a definition of “downwind” and for an explanation of the 30 km criterion). EDGAR is just used for the presence of an emission area, not for evaluation. Note that we do not attempt to optimize the wind direction given the uncertainty in the emitter location in EDGAR and given the relatively large area of the cells of this inventory (1 square degree). Other sources of information would be needed to do it properly.

2.3.2 Global IFS CO₂, CH₄ and NO_x inversion

The Copernicus Atmosphere Monitoring Service employs a four-dimensional variational (4D-Var) data assimilation system within the ECMWF Integrated Forecasting System (IFS). This system integrates atmospheric composition observations with model forecasts to produce accurate analyses and forecasts of atmospheric constituents such as aerosols and trace gases. Recently a joint state/emission optimisation system has been implemented in the IFS 4D-Var algorithm ([McNorton et al., 2022](#)).

The CAMS inversion utilises 12-hour assimilation windows, specifically from 09:00 to 21:00 UTC and from 21:00 to 09:00 UTC. An incremental 4D-Var method is employed, involving two minimizations at different spectral truncations: T95 (approximately 210 km) and T159 (approximately 110 km). This strategy balances computational efficiency with the need for detailed spatial resolution in the optimization. The 4D-Var minimisation uses tangent linear and adjoint models of a simplified chemistry mechanism based on the NO_x photochemical equilibrium. The system assimilates a diverse array of satellite observations, including total column measurements of carbon dioxide (CO₂) (OCO2), carbon monoxide (CO) and methane (CH₄) (TROPOMI, IASI), tropospheric nitrogen dioxide (NO₂) (TROPOMI, OMI), aerosol optical depth (AOD), and both total column and profile data for ozone (O₃).

The global IFS CO₂ inversion product described in this deliverable is obtained by multiplying the posterior NO_x inversion product by the NO_x/CO₂ emission ratio of the prior CAMS CAMS_GLOB_ANT v5.3 inventory.

The global daily NO_x, CH₄ and CO emission inversions have been performed for the years 2019 and 2022. They use as prior the CAMS_GLOB_ANT v5.3 inventory and prior errors based on the CORSO W1 product provided by TNO.

2.3.3 Point and area sources emissions compared with IFS CO₂ inversion

The comparison of point-source emissions between IFS and OCO results in 2019 and 2022 shows very large differences. Emission retrievals from OCO are much higher than the results of IFS, and the correlation is weak (Figure 2.3.1(a)). The point sources with the largest emission discrepancy are located in northern China, with a maximum difference reaching -21,394 kg CO₂/s (Figure 2.3.1(b)). The reasons for such a large discrepancy may include: (1) uncertainties in the conversion process from NO_x to CO₂, and (2) the observed plume

CAMEO

emissions from OCO potentially originating from multiple point sources, which, due to limited information, makes it challenging to accurately identify the exact emission location.

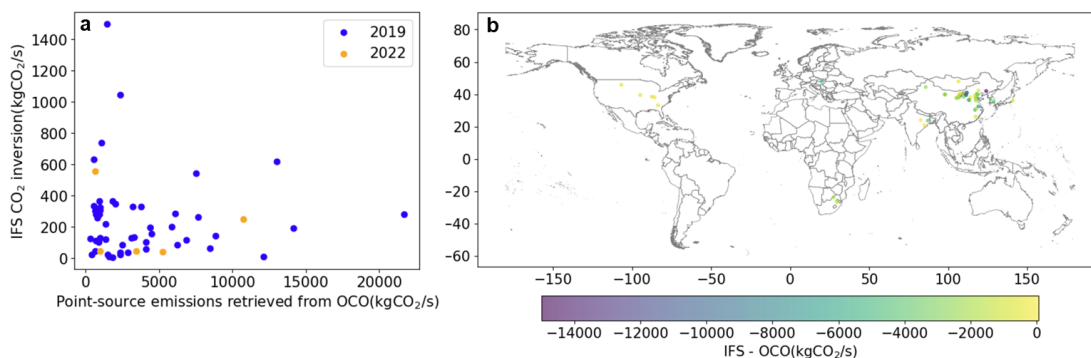


Figure 2.3.1 a) Comparison of point-source CO_2 emissions between IFS and OCO inversion results. a, scatter plot of point-source CO_2 emissions. b) Spatial distribution of the differences (IFS minus OCO inversion for both years).

We also interpolated the gridded emissions of IFS to a resolution of $0.1^\circ \times 0.1^\circ$ for comparison with EDGARv8.0 and GRACED in 2019. The spatial determination coefficient (R) between IFS and GRACED at 0.1° is 0.24, whereas it is only 0.20 between IFS and EDGAR. As shown in Figure 2.3.2, the spatial pattern of IFS exhibits significant differences compared to GRACED and EDGAR in major countries such as the US, Germany, India, and China.

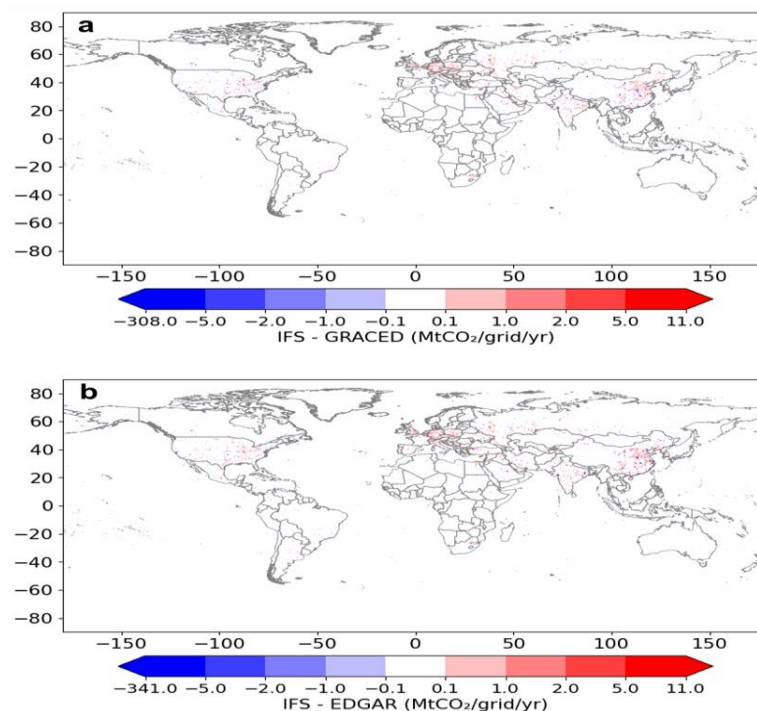


Figure 2.3.2 Difference of gridded CO_2 emissions between IFS, EDGAR and GRACED at 0.1° in 2019. a, IFS minus GRACED. b, IFS minus EDGARv8.0.

2.4 Evaluation of CH₄ inversions

2.4.1 Global inversions models

2.4.1.1 Global CH₄ inversions of the Global Carbon Project

The ensemble of inversions spans from 2000 to 2020 and contains seven different inverse systems for 18 inversions. This ensemble of inversions gathers various chemistry transport models, differing in vertical and horizontal resolutions, meteorological forcing, advection and convection schemes, and boundary layer mixing. Including these different systems is a conservative approach that allows to cover different potential uncertainties of the inversion, among them: model transport, set-up issues, and prior dependency. Most inversions except four, use common prior emission maps for natural and anthropogenic prior emissions divided into 12 sectors, particularly the EDGAR v6 inventory for prior fossil fuel emissions ([Crippa et al., 2021a](#) extrapolated to Jan 1st, 2021). The inversions assimilating surface stations mixing ratios observations provide results since 2000 (hereafter called SURFACE inversions), and those assimilating satellite observations from column CH₄ measurements (XCH₄) of the GOSAT satellite provide results since 2009, the year when GOSAT was launched (hereafter referred to as GOSAT inversions). Inversion results were gridded into 1° by 1° monthly emission maps. Fossil fuel emissions from the “oil & gas” and “coal” sub-sectors were separated from other sources in each grid cell by taking the fractions that these two sub-sectors represent in each grid cell, based on the prior emission fields. Then, emissions were aggregated nationally using a country mask (Klein Goldewijk et al., 2017).

These inversions differ from those used in Deng et al. (2022) based on the global methane budget 2020 ([Saunois et al. 2020](#)). The ensemble of inversions (hereafter called GCP2020) was based on earlier versions of prior anthropogenic emissions from EDGAR with different versions (EDGAR v4.2 and EDGAR v4.3.2) used among inversion runs. As a result, some significant differences between the previous and new ensembles of inversions are expected.

2.4.1.2 Global IFS CH₄ inversion

See Section 2.3.2.

2.4.2 CAMEO data collected and processed for inversions evaluation

2.4.2.1 Bottom-up inventories

We only considered CH₄ emissions from the fossil fuel sector for all bottom-up inventories (**Table 2.4.1**). We included EDGARv6 and GAINS but keep in mind here that these two inventories were used as a prior for the GCP inversions (see **section 2.5.3**), thus cannot provide an independent evaluation of the results from this inversion. The fossil fuel sector comprises all sources related to the production and distribution of coal, oil, and gas fuels. Emissions of CH₄ from sources involving the combustion of fossil fuels (e.g., electricity generation, chemical industry) are marginal, representing on average 2.6% of the total fossil CH₄ emissions (considering all bottom-up inventories and countries analyzed in this study). Therefore, they are omitted here. **Table 2.4.1** presents the oil, gas, and coal emission sectors and subsectors from the different bottom-up emission inventories used in this work. Each inventory is shortly described below.

- **UNFCCC emissions reported per country** were extracted for oil, gas, and coal subsectors from the latest inventory accessible in the Greenhouse Gas Inventory Database (https://di.unfccc.int/detailed_data_by_party). Annex I countries report emissions yearly, while non-Annex I countries report less frequently. We use data from National Inventory Reports (NIR) for all Annex I countries and national communications (NCs) / biennial update reports (BURs) for non-Annex I countries.

CAMEO

- **GFEI inventory** ([Scarpelli et al., 2022](#)) reports emissions from 2010 to 2019. The emissions are based on NIR v2021 (UNFCCC report published/as available in 2021) for the Annex I countries but a composite methodology for the non-Annex I countries. For countries with no reported data after 2000 from UNFCCC (i.e., NCs/BURs), a Tier 1 approach was applied. This approach combined default emission factors from IPCC and annual activity data from the US Energy Information Administration (EIA). On the other hand, for those non-Annex I countries that had reported emissions to UNFCCC after 2000, the reported values were adjusted and filled for missing years using the EIA data.
- **Community Emissions Data System (CEDS)** inventory corresponds to the latest version, CEDS v2021-04-21, released on May 5, 2021. This version contains CH₄ emissions from 1970 to 2019. A description of the methodology can be found in [Hoesly et al., 2018](#). Briefly, CEDS deploys a two-step approach. First, it creates a set of default emissions using activity data from international datasets and emission factors from other global inventories. For the coal sector, default CH₄ emissions are directly taken from EDGARV6 and interpolated using population data from United Nations and World Bank for missing values. The oil and gas sector's emissions are based on the combination of EDGAR and GAINS datasets with the missing years interpolated using production data from IEA (International Energy Agency) and BP (British Petroleum) energy statistics. Second, for countries having a regional inventory, the default emissions factors and emissions are scaled to match the corresponding sectoral estimates from that regional inventory. While this is the general methodology, specific revisions have been made over the years for certain countries/sectors (CEDS, 2021), which are unclear and beyond the scope of this study.
- **GAINS global inventory** has yearly emissions from 1990 to 2020. A description of the methodology can be obtained from [Höglund-Isaksson 2012](#) and [Höglund-Isaksson et al. 2020](#). Activity data (fossil fuel production) is obtained from the International Energy Agency –World Energy Outlook (IEA-WEO) New policies scenario v2018. Therefore, values after 2017 are projections, not actual activity. In regard to emissions factor, values for coal mining are obtained from a combination of national reporting to UNFCCC (either NIR or BUR) where available, IPCC default values, and specific studies for China (Peng et al. 2016, China BUR to UNFCCC 2017, Miller et al. 2019, Sheng et al. 2019). For abandoned mines, it is taken directly from the NIR submitted to UNFCCC for Annex I countries and assumed as 10% of mining emissions for non-Annex I countries. For the oil and gas sectors, emission factors are based on Höglund-Isaksson (2017) for all countries with updated information for the USA (Zavala-Araiza et al. 2015, Omara et al. 2016, Alvarez et al. 2018) and Russia (Huang et al. 2015, Elvidge et al. 2016).
- **EDGARv6 inventory** reports emissions from 1970 to 2018. It is the prior inventory for the new ensemble of global inversions discussed above. In this version of EDGAR ([Crippa et al., 2021b](#)), activity data is obtained from international energy statistics from the IEA v2019. The source of emissions factors seems similar to those used in version v4.3.2 except for emissions from venting in oil and gas sectors which are based on updated information from UNFCCC v2020, EPA v2020, and Höglund-Isaksson (2017). In EDGARv4.3.2 ([Janssens-Maenhout et al., 2019](#)), activity data is primarily from World Coal Association v2016 and IEA v2014, supplemented with additional region-specific datasets. Emissions factors are mainly sourced from IPCC default values and UNFCCC NIRs v2014 and v2016.
- **IEA global inventory datasets**: We collected two datasets, one with a time series (1990-2015) of emissions from fossil fuel sources ([IEA, 2020](#)) and another one for the year 2020 ([IEA, 2021](#)). The first dataset (hereafter referred to as IEA) comprising the time series is

CAMEO

available at five years intervals. We interpolated between each timestep to produce yearly emissions. In this dataset, methane emissions for the fossil sector are directly taken from EDGARv4.3.2 ([IEA, 2022](#)). The second dataset (hereafter referred to as IEA_2020) includes emissions only for oil and gas activities. The activity data (i.e., production and consumption) for the oil and gas sector are based on IEA energy statistics. For fugitive emissions (i.e., leakage and venting), the emission factors are based on US emissions intensities from EPA inventory v2021, which are scaled for respective countries using relevant country-specific data (IEA, 2022b). Flaring emissions are estimated based on country-specific combustion efficiencies using country-specific data on production type, company type, wind speed, and regulatory policy (IEA, 2022b). Further, it also includes emissions from ultra emitters (sporadic emission events with rates greater than 20 tCH₄ per hour) based on data from the Methane Watch - Kayrros (www.kayrros.com/methane-watch), the same data source as the one we used here. However, their ultra-emitters dataset corresponds to January 2021; here, we present updated data for June 2021 ([Lauvaux et al., 2022](#)).

- **U.S. EPA inventories** also comprise two datasets. The first one contains global emissions every five years from 1970 until 2015, with future projections up to 2050, from which we calculate yearly emissions (up to 2020) by linearly interpolating values between two timesteps ([USEPA, 2019](#)). The emissions are directly taken from UNFCCC NIRs v2018 for A-1 and relevant NCs/BURs for NA-I countries (USEPA, 2019b). The missing years are filled with activity data from EIA v2018. For countries with no year from UNFCCC, emissions factors are taken from IPCC 2006 default values and combined with the EIA data. For China, coal sector emissions are based on UNFCCC NCs (v1994 and v2005) and Lixin 2016, supplemented with EIA v2018 activity data to interpolate missing years. The second dataset contains yearly emissions from 1990-2020 only for the U.S., separating coal, oil and gas sectors ([USEPA, 2022](#)) and developed using a combination of Tier 3 and Tier 2 approaches (USEPA, 2022b). Activity data are primarily based on production data from EIA v2021 for the coal sector and Enverus v2021, supplemented with other national datasets for the oil and gas sectors. Emission factors for the coal sector are based on mine-specific data from EPA's national Greenhouse gas reporting program (GHGRP) for underground mines and older basin-specific datasets for surface mines. For oil and gas, these are sourced from multiple national datasets (Table S4). For the U.S., we used this inventory instead of the global EPA dataset.

Table 2.4.1. Bottom-up and top-down emission inventories of fossil fuel sources used in this study.

Emission inventory	Time period	Resolution	Sector/Subsector	Coverage	Reference
Bottom-up inventories					
UNFCCC	1986 - 2019	Yearly	Coal, Oil and gas	Global	UNFCCC 2021
GFEI	2010-2019	Yearly	Coal, Oil, Gas	Global	Scarpelli et al. 2022
CEDS	1970 - 2019	Yearly	Coal, Oil, Gas	Global	O'Rourke et al. 2021
EDGARv6	1970 - 2018	Yearly	Coal, Oil and gas	Global	Crippa et al., 2021
GAINS	1990-2020	Yearly	Coal, Oil, Gas	Global	Höglund-Isaksson et al. 2020
EPA	1990 - 2050	Every 5 years**	Coal, Oil, Gas	Global	USEPA, 2019
	1990 - 2019	Yearly	Coal, Oil, Gas	U.S.A.	USEPA 2022
IEA	1990 - 2015	Every 5 years*	Fossil	Global	IEA 2020
IEA 2020	2020	Yearly	Oil, Gas	Global	IEA 2021
Top-down approaches					
SURFACE Inversions N = 12*	2000 - 2020	Monthly fluxes aggregated to yearly	Coal, Oil and gas	Global	Saunois et al. (2023)
GOSAT Inversions N = 4 *	2010 - 2020	Monthly fluxes aggregated to yearly	Coal, Oil and gas	Global	Saunois et al. (2023)
Ultra emissions >2000 events	2019-2020	Yearly	Oil and gas: ultra emitters	Single events	Lauvaux, et al., (2022)

2.4.2.2 Ultra-emitters from TROPOMI

We collected estimations of ultra-emission point sources based on plume inversions applied to all detectable large plumes from TROPOMI following the methodology of Lauvaux et al. 2022. Assuming that sporadic ultra-emissions are not captured by global inversions, we collected and analysed hundreds of very large releases from atmospheric methane images sampled by TROPOMI. This effort captured point source emissions exceeding a release rate of 20 tons/hour, predominantly originating from oil and natural gas production or transmission facilities. Due to the sensitivity limitations of the TROPOMI instrument, detecting atmospheric column CH₄ enhancements from a single point source faces challenges, influenced by the overlap of plumes from multiple adjacent natural gas facilities and complex spatial gradients. Consequently, we followed the methodology of [Lauvaux et al., 2022](#) by adopting an automated plume detection algorithm based on machine learning, coupled with the Lagrangian particle dispersion model HYSPLIT (Hybrid Single-Particle Lagrangian Integrated Trajectory model), to quantify the associated emissions for each detected plume enhancement globally. Therefore, assuming that sporadic ultra-emissions are not captured by global inversions, this study incorporates TROPOMI-based inversion data on ultra-emitters emissions from 2019 to

CAMEO

2022 as one of its input data sources. The data encompasses the coal and oil and gas ultra-emitters, with a daily temporal resolution, detailing 654 large-scale coal leak events and 2322 large-scale oil and gas leak events, including point source monitoring emissions and geographical coordinates. The sector classification within the data aligns with the definitions used in this study (Figure 2.4.1).

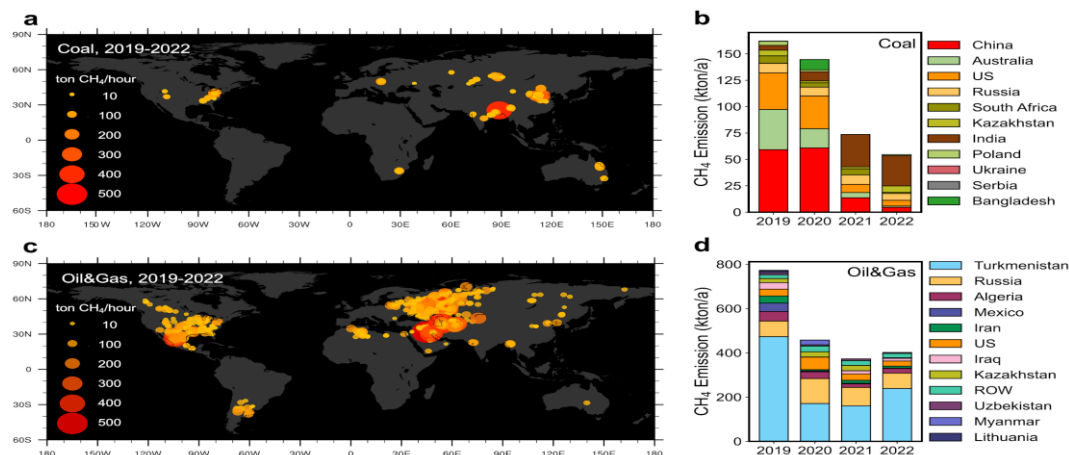


Fig. 2.4.1. Global map of coal and oil and gas ultra-emitters from TROPOMI collected for the CAMEO project. *a*, Spatial distribution of coal ultra-emitters. *b*, Country-level annual emissions from coal ultra-emitters. *c*, Spatial distribution of oil and gas ultra-emitters. *d*, Country-level annual emissions from oil and gas ultra-emitters. (Circles are scaled according to the emission rate of the ultra-emitters).

2.4.2.3 Basin-level high-resolution inversions of TROPOMI images

We used a new dataset of methane emissions from the extraction of fossil fuels for 14 major basins across the world. These estimates are based on high resolution localized inversions (Peng et al., 2023) assimilating all possible high-resolution daily atmospheric methane concentrations collected by the Sentinel-5P/TROPOMI (TROPOspheric Monitoring Instrument) over each of these basins individually. TROPOMI-based methane concentrations have been widely used in recent times, under various methodological schemes to estimate emissions across various spatial domains (Chen et al., 2023; Cusworth et al., 2022; Lauvaux et al., 2022; Peng et al., 2023; Sadavarte et al., 2021; Shen et al., 2023; Varon et al., 2023; Veefkind et al., 2023; Zhang et al., 2020). This analysis covers large emitting basins (Table 2.4.2), contributing nearly one-fourth of the global methane emissions from the fossil-fuel sector, with shares from individual basins ranging from 30% to 100% of the respective national fossil-fuel emissions (Fig. 2.4.2) according to different bottom-up inventories. Moreover, for these basins, the suitability of the TROPOMI product is among the highest because of its relatively higher coverage in mid-latitude countries than high-latitude countries (Gao et al., 2023).

CAMEO

Table 2.4.2 List of basins for which high resolution inversion-based emissions have been collected for the CAMEO project, and the regions they originate from. See Figure 2.4.3 for their locations.

Sl. No.	Broad region	Country / Sub-region	Basin	Type
1	Middle East	Iran	East Iran	Oil and gas
2			West Iran	Oil and gas
3		Iraq	Iraq	Oil and gas
4		Kuwait	Kuwait	Oil and gas
5	Central Asia	Turkmenistan	East Turkmenistan	Oil and gas
6			West Turkmenistan	Oil and gas
7		Uzbekistan	South Uzbekistan	Oil and gas
8	Eastern Asia	China	Shanxi	Coal
9	North America	United States of America (USA)	Appalachian	Mixed
10			Permian	Oil and gas
11			Anadarko	Oil and gas
12	Africa	Algeria	Algeria	Oil and gas
13		South Africa	South Africa	Coal
14	Oceania	Australia	Bowen-Surat	Coal

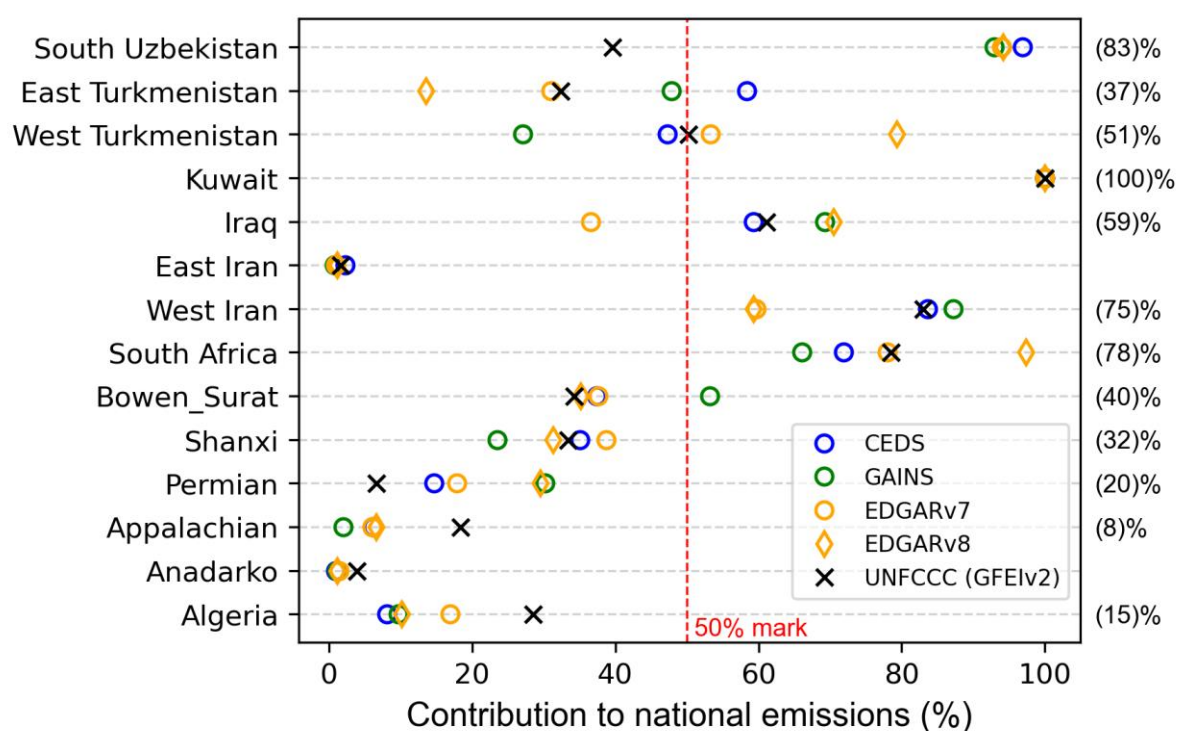


Figure 2.4.2. Contribution to national fossil fuel emissions for each basin for which we have an independent emissions estimates based on regional inversion of TROPOMI images.

Contribution of emissions over the basin area to the total national fossil-fuel emissions based on estimates from different bottom-up inventories averaged during 2019-2020. Values in the brackets denote the mean contribution from all bottom-up inventories for basins with contribution $\geq 5\%$. For Turkmenistan, there are two basins, East and West.

The estimates based on localized inversions using the TROPOMI methane column (XCH_4) are presented for 14 fossil-fuel basins categorized as oil and gas, coal, and mixed, further lumped into 6 broad regions (Figure 2.4.3). All basins combined sum up to a mean emission

CAMEO

of 28.0 ± 2.7 Mt/yr during 2019-2022. As per the Global Methane Budget 2024 Saunio et al., 2024, total methane emissions (averaged over 2010-2019) from fossil fuel production and use are 120 Mt/yr and 115 Mt/yr based on bottom-up inventories and global inversions, respectively. Thus, emissions over these basins estimated through localized inversions represent nearly one-fourth of the global methane emissions from the fossil fuel sector.

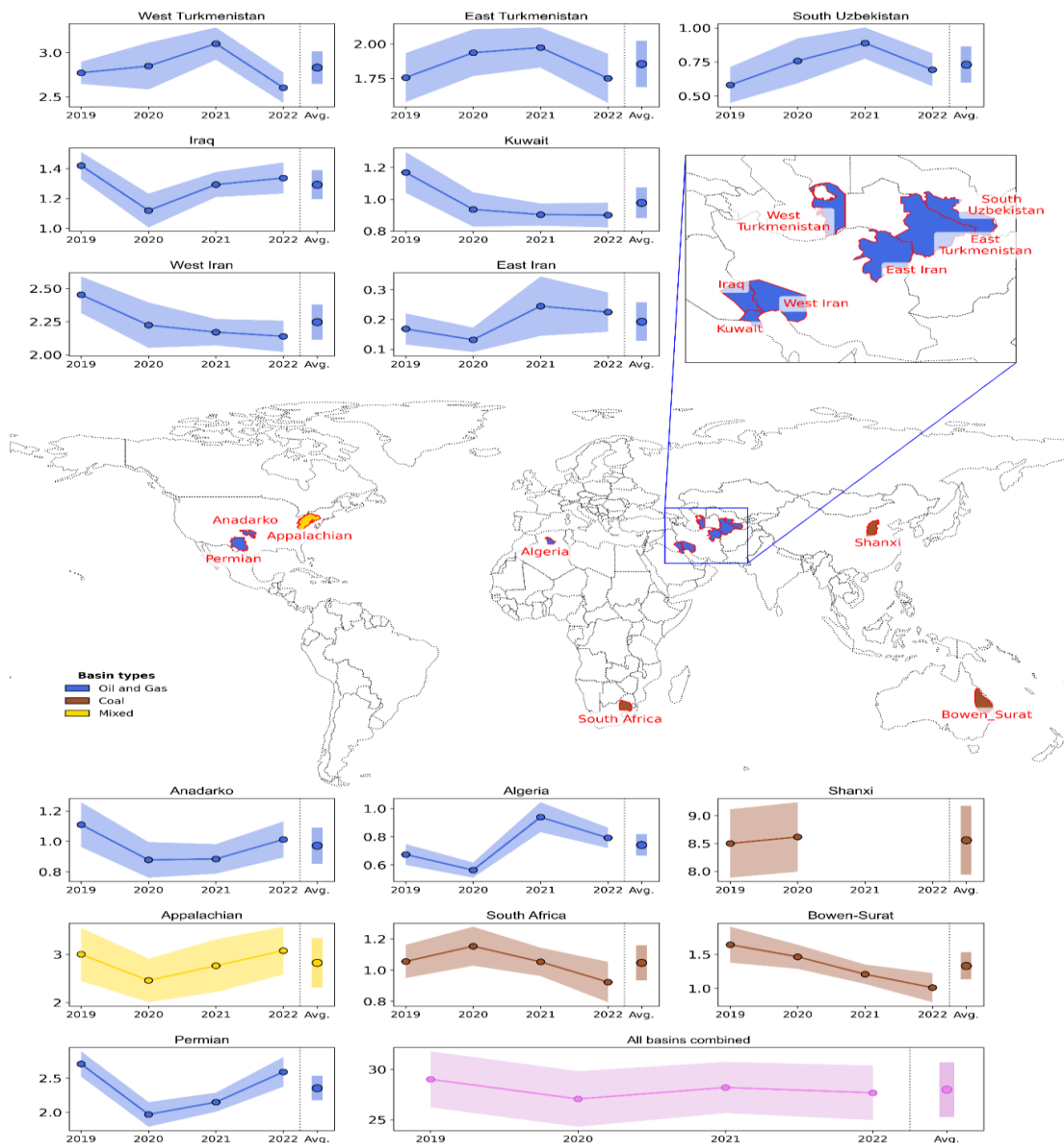


Figure 2.4.3. Methane emissions (MtCH_4/yr) over selected fossil fuel basins from regional high-resolution inversions based on quasi-weekly exploitable TROPOMI images. Blue polygons represent oil-gas basins, brown is for coal basins, and yellow for mixed basins. The line represents the annual mean time series of emissions and the shaded region represents the 95% confidence interval. The pink dot and shaded bar at the right represent the mean and confidence interval for emissions averaged during 2019-2022.

We include a total of three coal basins. The highest emissions come from the basin in Shanxi province in China, emitting around 8.5 ± 0.6 Mt/yr followed by relatively lower emissions from the Bowen-Surat basin in Australia and a South African basin, emitting 1.3 ± 0.2 and 1.0 ± 0.1 Mt/yr, respectively. Emissions from the Shanxi basin are only processed for two years, 2019

CAMEO

and 2020. We also include one mixed basin, Appalachian, located in North America emitting a total of 2.8 ± 0.5 Mt/yr with 42% from oil and gas, and 58% from coal production. There are seven oil and gas basins located in the Middle East (four) and Central Asia (three) with the total estimated mean emissions (average of 2019-2022) of 10.1 ± 0.9 Mt/yr, and a range from 0.2-2.8 Mt/yr across individual basins. The highest emissions arise from the West Turkmenistan basin (2.8 ± 0.2 Mt/yr), followed by West Iran (2.2 ± 0.1 Mt/yr), East Turkmenistan (1.9 ± 0.2 Mt/yr), Iraq (1.3 ± 0.1 Mt/yr) and Kuwait (1.0 ± 0.1 Mt/yr). Lower emissions come from South Uzbekistan (0.7 ± 0.1 Mt/yr) and East Iran (0.19 ± 0.06 Mt/yr). Cumulatively, basins in Turkmenistan (46%) and Iran (24%) contribute around 70% of total emissions from these countries. Another couple of oil and gas basins are located in North America, emitting 2.4 ± 0.2 Mt/yr from Permian and 1.0 ± 0.1 Mt/yr from Anadarko, respectively. Finally, the Algerian basin located in Africa emits 0.7 ± 0.1 Mt/yr.

The robustness of our basin-level estimates from high-resolution localized inversion has been validated previously, which showed the results for the Shanxi province agreeing well with the ground-based measurements. Here, we further compare our estimates to other existing localized inversions over the Permian, Bowen, and Algerian basins (Fig. 2.4.3). We found our estimates for the Permian well within the range of other existing studies with similar spatial coverage and time of reporting. In Varon et al., 2023¹⁹, the posterior emissions from TROPOMI-based inversions are compared with independent tower and aircraft-based measurements, further strengthening the validity of our estimates over the Permian basin. Moreover, in the absence of existing studies for other basins, we believe this comparison over the Permian (among the largest oil and gas producers in the world) renders enough credibility to our estimates over other basins. Estimates for the Bowen and Algerian basins from Sadavarte et al., 2021²³ and Naus et al., 2023²² are 0.6 ± 0.1 and 0.16 ± 0.06 Mt/yr, respectively. These are nearly half of our study but may not be directly comparable. For Bowen, the spatial coverage was smaller than in this study. For Algeria, the previous study by Naus et al. 2023²² used a coarser resolution ($0.2^\circ \times 0.2^\circ$) for TROPOMI input compared to this study ($0.1^\circ \times 0.1^\circ$) and simulated only for 2020, which had significantly lower emissions than other years. Regarding the annual emissions trajectory from 2019 to 2022 (Fig. 2.4.3), 9 out of the 14 basins showed a dip in 2020, potentially due to the effect of the worldwide closures during the COVID-19 pandemic. Basins showed mixed directions of emissions change after 2020, with most basins showing either stable or decreasing emissions till 2022 in general, except basins in North America and Iraq which showed increasing emissions. For each basin, we estimated the absolute and relative emission reductions in 2020 compared to 2019. In relative terms, the emission changes ranged from -9 to -27% across the basins, corresponding to absolute emission changes of -0.04 to -0.7 Mt/yr. The highest reduction (-27%) was for the Permian basin, corresponding to an absolute emission change of -0.7 Mt/yr. However, a large percentage reduction does not necessarily mean a substantial absolute reduction. For example, East Iran, Anadarko, Kuwait, and Iraq showed relative emission changes of around -20% but with absolute emission changes of only -0.04, -0.2, -0.2, and -0.3 Mt/yr respectively. Other basins, including West Iran and Bowen-Surat, showed lower relative reductions (-9% and -11%, respectively) but comparable absolute reductions (-0.2 Mt/yr each). Taken together, these 9 basins had an emission reduction of 2.6 Mt/yr in 2020 compared to 2019.

After the dip in 2020, emissions remained nearly stable at 2020 levels up to 2022 for Kuwait and West Iran (Fig 2.4.3). However, for basins in North America (Appalachian, Permian, and Anadarko), emissions rebounded to 2019 levels, gradually by 2022 (Fig. 2.4.3). Emissions from basins in Iraq also rebounded closer to the 2019 level but with an immediate rise in 2021

followed by much slower growth in 2022. Emissions from low emitting basins, such as East Iran and Algeria, showed a sudden increment in 2021 surpassing the 2019 levels, followed by nearly stable to declining emissions in 2022. Only emissions from the Bowen-Surat basin showed a continued decline up to 2022.

In contrast, unlike the basins discussed above, oil and gas basins in Turkmenistan, South Uzbekistan, and the coal basin in South Africa had no emissions reductions in 2020. For both basins in Turkmenistan, among the large emitters, emissions increased from the 2019 level to peak in 2021 and then declined in 2022. A similar trajectory is also found for the low-emitting basin in South Uzbekistan. Unlike other basins, Turkmenistan and Uzbekistan have larger contributions from midstream and downstream activities ^{5,26}. Thus, emissions may correlate more to consumption patterns than production. Finally, for a moderately high-emitting coal basin in South Africa, emissions increased by 10% (or 0.1 Mt/yr) in 2020 relative to 2019, followed by a decline of 13% (or 0.1 Mt/yr) in 2022 compared to 2019.

2.4.3 Results of inversions comparisons

2.4.3.1 Evaluation of global CH₄ inversions against CAMEO gridded bottom-up inventories

We present here only results for the comparison for fluxes over the last decade. Results for different versions of UNFCCC inventories and trends per fossil CH₄ emission sub-sector can be found in Tibrewal et al. 2024. Figure 2.4.4 shows a 2011-2020 comparison of fossil fuel CH₄ emission estimates from bottom-up and top-down approaches for selected countries. Regarding bottom-up approaches, the first bar from the left represents the official national emissions reported to the UNFCCC, followed by inventory estimates from international organisations described above. The last two bars are estimates from GCP inversions approaches based on surface stations and GOSAT atmospheric observations, respectively. The UNFCCC emissions correspond to the mean of reported values between 2011 and 2020 from the latest NIR (i.e., 2022) for Annex I countries. For Non-Annex I countries, it represents the average of values from any reports available within this period. SURFACE and GOSAT emissions correspond to the mean of inversions from 2011 to 2020. Finally, we added nationally aggregated estimates of ultra-emitters on top of each bottom-up inventory (red bar) since emissions from ultra-emitter events (sporadic >25 tCH₄.h⁻¹ leaks) are not considered in bottom-up inventories, except for the IEA 2020 oil and gas inventory that already used ultra-emitters emissions estimates from the same data source than in this study. The results are presented for each country in the following.

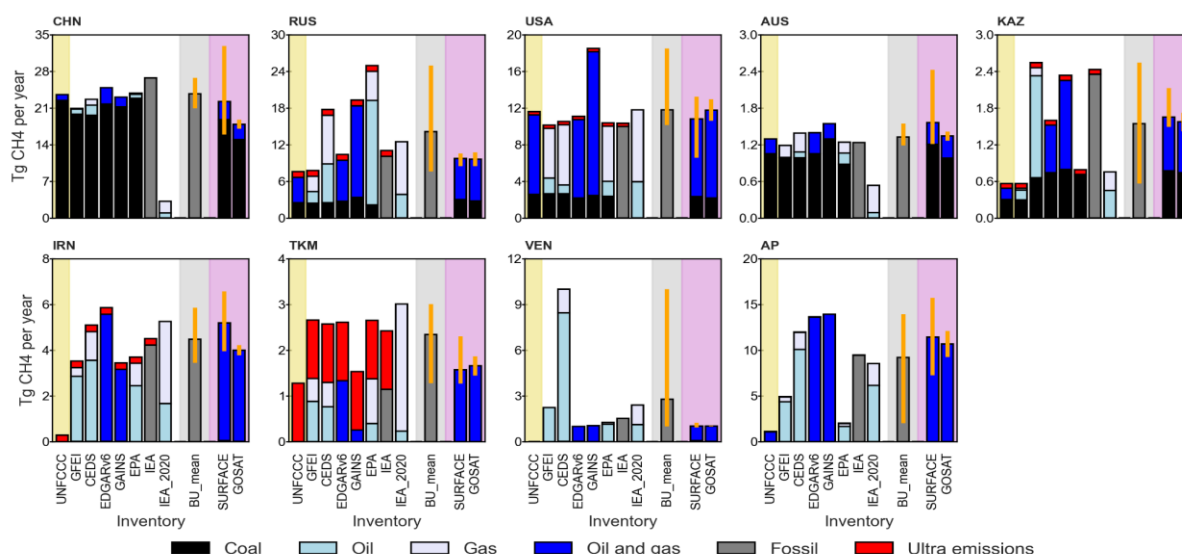


Figure 2.4.4. Fossil fuel CH₄ emissions from top-down and bottom-up approaches during 2011-2020. UNFCCC emissions (with yellow shaded background) represent the mean of available country reports during the same period. Inversion emissions (with pink shaded background) from SURFACE and GOSAT correspond to the average of inversions from 2011 to 2020. Error bars denote minimum and maximum values from inversion ensembles. On top of all bottom-up inventories are emissions from ultra emitters (red bars, as diagnosed from S5P TROPOMI measurements for 2019-2020 (Lauvaux et al. 2022)). Note that there is no reported emissions for IRN, VEN, and most countries within AP (Arabian Peninsula countries) from UNFCCC during exactly the same period, and that IEA_2020 only reported emissions from the oil and gas sector.

China is the most significant contributor to methane emissions from fossil fuels, with average emissions of 24 (21-27) Tgyr⁻¹ from the bottom-up and 22 (16-33) Tgyr⁻¹ from top-down estimates during 2011-2020. The coal sector is the dominant contributor (~80%) to total emissions from fossil fuels. Average estimates of total fossil fuels emissions from bottom-up inventories (including UNFCCC) agree well with SURFACE inversions, but GOSAT estimates are 20% lower. Regarding UNFCCC estimates, the total fossil fuel emissions are similar to the average bottom-up estimate but 7% higher than average inversion emissions. The lower 2011-2020 estimate from atmospheric inversions compared to UNFCCC emissions is consistent with the 2013-2017 results reported by [Deng et al. 2022](#) with the previous inversion ensemble from GCP ([Saunois et al. 2020](#)). At the sub-sectoral level, UNFCCC estimates from the oil and gas sector are at least 40% lower than other bottom-up estimates.

Russia emitted an average of 14 (8-25) Tg yr⁻¹ (bottom-up including ultra emitters) and 10 (9-11) Tg yr⁻¹ (top-down) during 2011-2020, with 80% contribution from the oil and gas sector. Ultra emissions contributed roughly 7%. Large disagreements exist among the bottom-up estimates, mostly driven by differences in the oil and gas sector. The estimate from EPA is almost double the bottom-up average, and the ones from CEDS and GAINS are ~25% higher. IEA and EDGARv6 estimates are 25% lower than the bottom-up average, and those of UNFCCC and GFEI are ~45% lower. The total averaged emissions from inversions are ~30% lower than those from bottom-up inventories. All bottom-up inventories have higher or equivalent emissions than inversions except UNFCCC and GFEI. Lower emissions in UNFCCC compared to inversions were also reported previously ([Deng et al. 2022](#)) using an older version of inversions ([Saunois et al. 2020](#)). However, 2010-2015 inversion results from [Maasakkers et al. 2019](#) were reported to be 50% lower than UNFCCC 2012 estimates. This highlights a significant downward correction in the latest UNFCCC reporting, as noted by previous studies ([Zhang et al. 2021](#); [Qu et al. 2021](#)). Especially in regard to oil and gas sectors, the UNFCCC estimate agrees well with GFEI that used UNFCCC totals from 2021 but is ~50% lower than the mean of other bottom-up inventories. A lower estimate in UNFCCC compared to inversions and bottom-up arises from the downward correction of the Russian inventory in their 2019 report.

USA total average emissions of 12 (10-18) Tgyr⁻¹ (bottom-up) and 11 (7-13) Tgyr⁻¹ (top-down) are largely dominated by the gas sector (50%). Bottom-up and top-down approaches in the USA have comparable total emissions for 2011-2020 fossil fuel sectors, except for GAINS which has 50% higher emissions. GAINS emissions from the oil and gas sector are nearly double than other bottom-up inventories but similar to IEA 2020. Compared to regional inversions by [Maasakkers et al. 2021](#), estimates from the bottom-up (excluding GAINS and IEA 2020) and global inversions presented here are roughly 30% lower. Estimates from GAINS and IEA 2020 are more consistent with this regional inversion. However, IEA 2020 reports a larger share from the oil sector, which falls closer to the upper limit by regional inversions. In regard to UNFCCC, the reported emissions are slightly above other inventories but still quite comparable.

CAMEO

Australia emitted around 1.3 (1.2-1.5) Tgyr⁻¹ (bottom-up) and 1.5 (1.2-2.4) Tgyr⁻¹ (top-down), with 80% of emissions from the coal sector. Over 2011-2020, the averaged total fossil emissions from global inversions (SURFACE and GOSAT) were 15% higher than bottom-up approaches. In regard to the total fossil sector, estimates across all bottom-up inventories are consistent within 10%, except for GAINS which reported ~20% higher values than the bottom-up mean. For the coal sector, estimates across all bottom-up inventories are also within 10%, except for GAINS reporting ~30% higher values than the bottom-up mean. However, larger disagreements exist for the oil and gas sector, with estimates from UNFCCC, GFEI, and GAINS being 25-40% lower than the bottom-up mean but IEA 2020 and CEDS being ~60% and 20% higher, respectively.

Kazakhstan has total mean emissions of 1.5 (0.6-2.5) Tgyr⁻¹ (bottom-up) and 1.6 (1.4-2.1) Tgyr⁻¹ (top-down), with equal shares from the coal sector and oil & gas subsectors. While the average estimates for total fossil emissions from bottom-up and top-down approaches are nearly identical, there are significant disagreements among the inventories. Estimates from CEDS, GAINS, and IEA are 65% higher than the mean of all inventories, while those from UNFCCC, GFEI, and EPA are 55% lower, with both sectors contributing to this discrepancy. Emissions from the oil & gas sector for UNFCCC, GFEI, and EPA are ~80% lower than other bottom-up inventories, and those from the coal sector are 50% lower.

Iran, Turkmenistan, Venezuela, and the countries grouped in the Arabian Peninsula region (AP) emit CH₄ emissions uniquely from the oil and gas sector. Overall, estimates from SURFACE and GOSAT compare well, but there are large disagreements among the bottom-up estimates. For Iran, the average estimates from bottom-up, 5 (3-6) Tgyr⁻¹ and global inversions, 5 (4-7) are close, but disagreements exist among individual inventories. Estimates from CEDS, EDGARv6, IEA inventories and SURFACE inversions are roughly 50% higher than EPA, GAINS, GFEI inventories and GOSAT inversions. The bottom-up average estimate includes ~7% contribution from ultra emissions and no estimate from UNFCCC, as the last communication from Iran was in 2000.

Turkmenistan emits 2.5 (1.5-3.0) Tgyr⁻¹ (bottom-up including ultra-emissions) and 1.6 (1.3-2.3) Tgyr⁻¹ (top-down), having the largest share of emissions from ultra-emitters (50% of the total). It appears all other bottom-up inventories fail to account for ultra emissions as the estimates are almost 60% lower than IEA 2020, which already includes ultra emitters. After superimposing additional estimates for ultra emissions, the estimates across all bottom-up inventories come to an agreement, except for GAINS which still has 50% lower emissions than other bottom-up inventories. While the average bottom-up estimates after accounting for ultra emissions are 60% higher than estimates from the mean of global SURFACE and satellite inversions, they are still within the range from SURFACE inversion models.

For Venezuela, total average emissions from global inversions, 1.0 (0.7-1.5) Tgyr⁻¹ is roughly three times lower than bottom-up inventories, 2.8 (1.0-10.0) Tgyr⁻¹ due to significant disagreement among the bottom-up inventories. Estimates from EPA and IEA are 25-50% higher, GFEI and IEA 2020 are almost double, and CEDS is about ten times higher than global inversions. Estimates from GAINS and EDGARv6 are identical to global inversions. The mean emissions from SURFACE and GOSAT are quite similar, reporting ~1.0 Tgyr⁻¹ each.

For the Arabian Peninsula (AP) region, the average estimate from bottom-up inventories, 9 (2-14) Tgyr⁻¹ is 20% lower than global inversions, 11 (7-16) Tgyr⁻¹, again with a large disagreement among the bottom-up inventories. Emissions in EPA and GFEI are 80% and 50% lower and emissions in EDGARv6 and CEDS are ~30% higher than in other inventories. IEA 2020 estimates are close to the bottom-up average, with 20% lower emissions

CAMEO

than inversions. UNFCCC estimates are not included in the bottom-up mean as the values are only available for Kuwait and Saudi Arabia.

2.4.3.2 Evaluation of global CH₄ inversions against CAMEO basin-scale validation data

Unlike basin-scale 'localized' inversions presented in section 2.4.2, which have a high resolution, global inversions simulate the entire world at coarse resolutions. They primarily constrain the net methane fluxes from all sectors at national scale. The resultant gridded methane fluxes after inversion are distributed into different sectors based on their relative proportions in the prior inventories. The choice of the prior inventory may influence the sectoral posterior emissions from inversions. Thus, we consider two sets of global inversions, Glv1 and Glv2, using EDGARv6 and GAINS as priors, respectively (Tibrewal et al., 2024). Each set of global inversions comprises an ensemble of inversions with different inversion systems and input parameters (Saunois et al., 2020; Tibrewal et al., 2024).

Similar to bottom-up inventories, estimates from global inversions also report lower emissions (averaged during 2019-2020) than localized inversions for all basins combined (Fig 2.4.5). Glv1 underreports emissions by 34% compared to localized inversions during 2019-2020, nearly three times the underreporting from Glv2 (-12%). At the basin level, for Glv1, estimates are either considerably lower (-91% to -49%) or relatively similar (-4% to 23%) to localized inversions, leading to overall lower estimates. Even for Glv2, estimates are generally lower (-96% to -26%) across all basins except for Permian and Iraq, where the estimates from global inversions are nearly 3.3 and 4.5 times higher than localized inversions, respectively. This reflects the strong dependency of global inversions on prior inventories, as GAINS (prior inventory for Glv2) reported relatively larger emissions for the Permian and Iraq basins.

Compared to bottom-up inventories, emissions from global inversions are either comparable or towards the lower end of inventories across basins. This small discrepancy with a bias towards lower emissions in global inversions compared to bottom-up inventories for the fossil-fuel sector was also reported at the national level (Tibrewal et al., 2024) and the global level (Saunois et al., 2024). This general underestimation in global inversions compared to localized inversions and bottom-up inventories highlights the current limitation of global inversions in accurately resolving sub-sectoral and sub-regional emissions. This arises primarily due to poor observational constraints and uncertainties in prior emissions sources, discussed below.

The global inversions we used here for comparison assimilated methane concentrations based on a network of surface-based measuring stations and retrievals from the Greenhouse gases Observing Satellite (GOSAT) (Saunois et al., 2020). The surface observational network is sparse on a global scale and mostly concentrated in Europe and North-Eastern America, thereby mostly missing out on large emitting fossil fuel basins (Supplementary material of Tibrewal et al., 2024). Furthermore, the low data density and coarse spatial resolution of GOSAT limits its ability to identify methane hotspots over fossil fuel basins.

As mentioned above, global inversions are designed to solve for the total methane flux (i.e. with all emissions sources and sinks combined). It is hard to resolve sectoral emissions during inversion, particularly because many grids can have spatially overlapping emissions sources. Consequently, global inversions rely on the relative proportions from the prior inventories to disaggregate the total posterior emissions by sector. Therefore, both the magnitude and spatial distribution of emissions from the fossil fuel sector in the prior inventory can influence the gridded posterior emissions. The artifact of this simplistic disaggregating approach is evident in Figure 2.4.5. For all basins except Kuwait, the order of estimates between Glv1 and

CAMEO

Glv2 correlates with the order of estimates between their respective priors - EDGARv6 and GAINS. The influence of prior inventory on sectoral disaggregation of posterior emissions has also been highlighted previously (Cusworth et al., 2021; Tibrewal et al., 2024).

Such influence of overlapping emission sources can also be seen for regional inversions. Regional inversions lie in between localized and global inversions. While they can generate inversion-based estimates for the entire world, the inversion process is simulated over smaller regions spanning a few countries. Upon comparison with regional inversions over the Middle East and North Africa (Chen et al., 2023), estimates for Turkmenistan and Iraq show better alignment with emissions from this study than those for Kuwait, Iraq, and Algeria. This larger discrepancy in the latter set of countries may be attributed to the large share of emissions from co-located sources (livestock and waste) in the prior for these countries (Chen et al., 2023).

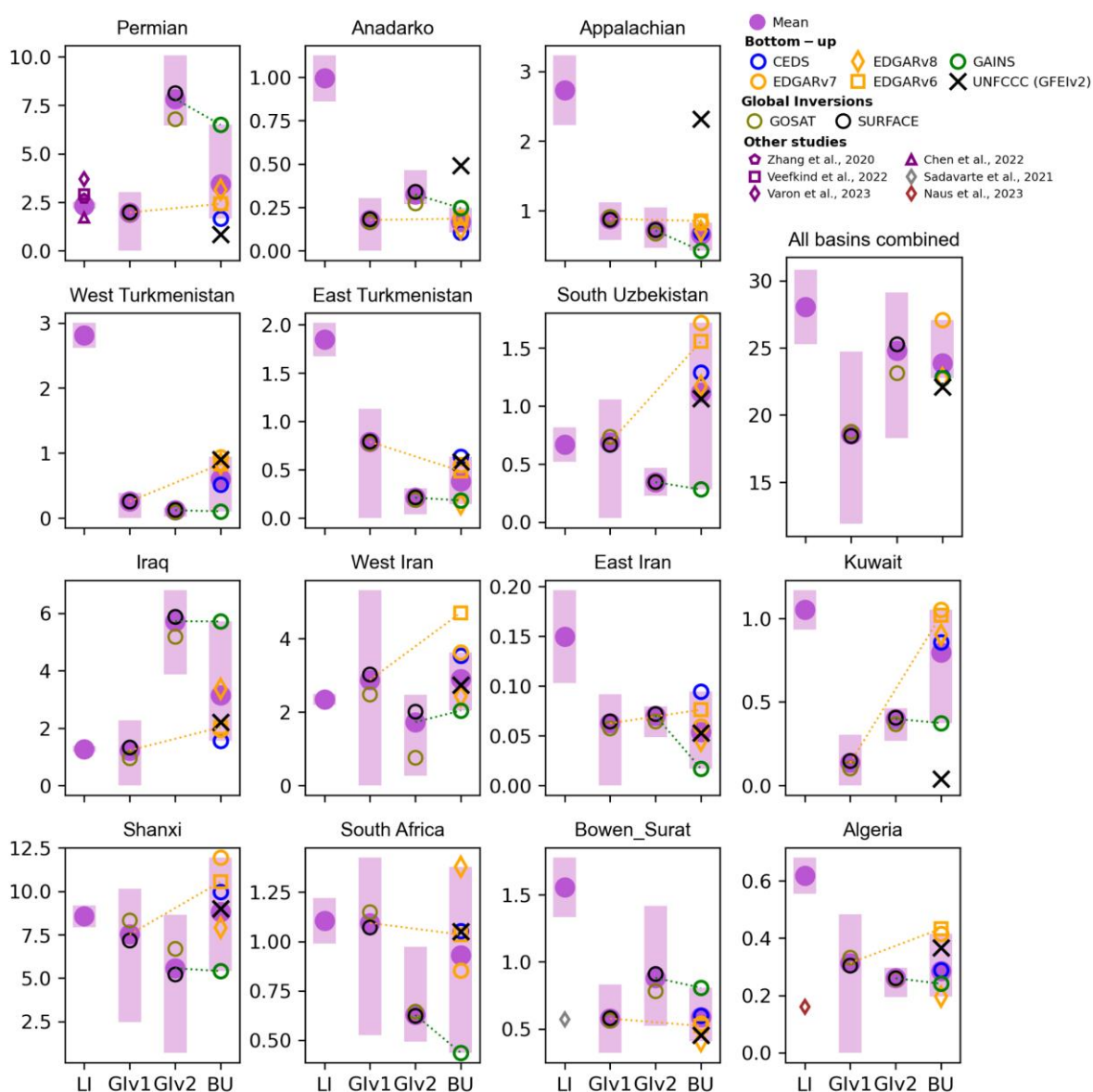


Figure 2.4.5. Methane emissions (Mt/yr) over major fossil fuel basins across different emission estimation approaches. For all approaches, emissions are averaged during 2019-2020 except for EDGARv6, for which only 2018 is shown. 'LI' represents the new TROPOMI-based localized inversions at basin levels from this study. Global inversions are from the Global Carbon Project and used for the

CAMEO

Global Methane Budget 2000-2020, 'Glv1' denotes global inversions with EDGARv6 prior, and 'Glv2' denotes global inversions using GAINS prior. 'BU' represents the set of global bottom-up inventories - CEDS, EDGARv6, EDGARv7, EDGARv8, and GAINS. Black 'x' represents the GFEIv2 bottom-up inventory, used as a proxy to UNFCCC estimates. The pink dots represent the mean from different estimates per approach type. The pink shaded bars represent the range (min and max) of estimates within the type of approach. For BU mean and range, EDGARv6, and GFEIv2 are not included. EDGARv6 is just shown as it is used as the prior for Glv1. The additional purple-edged symbols for the Permian, Bowen-Surat, and Algerian basins represent data from previous studies of localized inversions.

2.4.3.3 Evaluation of CAMEO IFS inversion against CAMEO validation data

Figure 2.4.6 gives a comparison between IFS-inversions for 2019 and 2022 and results from global inversion ensembles collected by Saunois et al. (2024) (in review) for selected high emitting countries and regions; Both prior and posterior inversion results are presented for IFS inversions. We can see that the global total emissions are comparable between IFS inversions 2019 and 2022, and GCP inversions. At regional scale, GCP and IFS have similar prior and posterior estimates for USA and Russia, IFS is lower than GCP for Canada and higher than GC in China. In Europe and Southeast Asia, IFS prior, posterior and GCP posterior emissions are comparable, although we do not have an uncertainty estimate for IFS inversions. In Africa, GCP inversions give a systematically higher emission total by about 30 Tg yr⁻¹, compared to both IFS inversions.

Total emissions of methane from inversions: CAMEO vs GCB

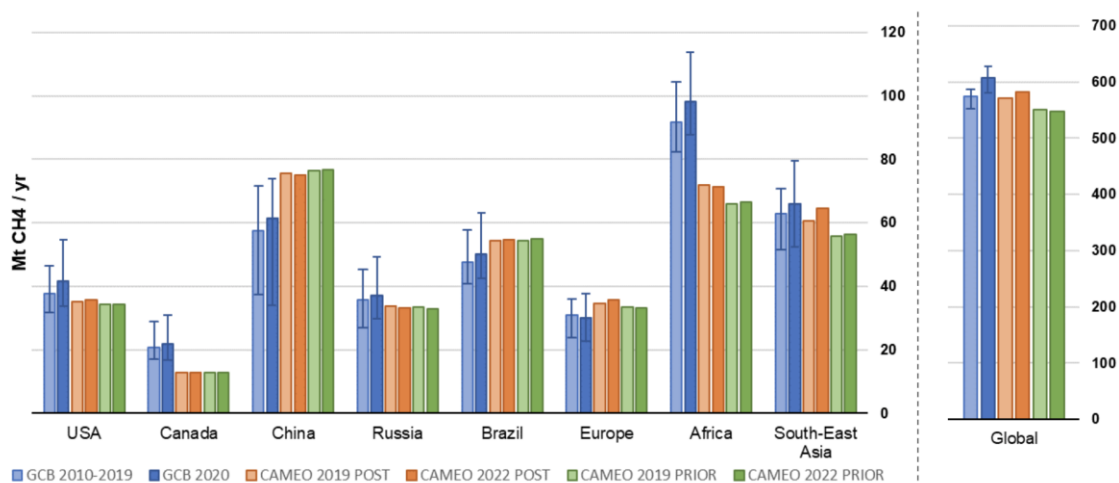


Figure 2.4.6. comparison between IFS-inversions for 2019 and 2022 (prior and posterior values) and results from global inversion ensemble of Saunois et al. 2024. Note that Saunois et al. 2024 has no inversion data available yet for the year 2022, the latest year being 2020.

Figure 2.4.7 shows a time series of daily CH₄ emissions from the IFS2019 and 2020 inversions. Although they have a similar mean seasonal amplitude, both inversions have positive spikes of emissions during some days which seem physically implausible and deserve better attention in future work, to understand their origin in the IFS inversion system. More detained comparisons have been performed for days when inversion spikes are present in the IFS inversions.

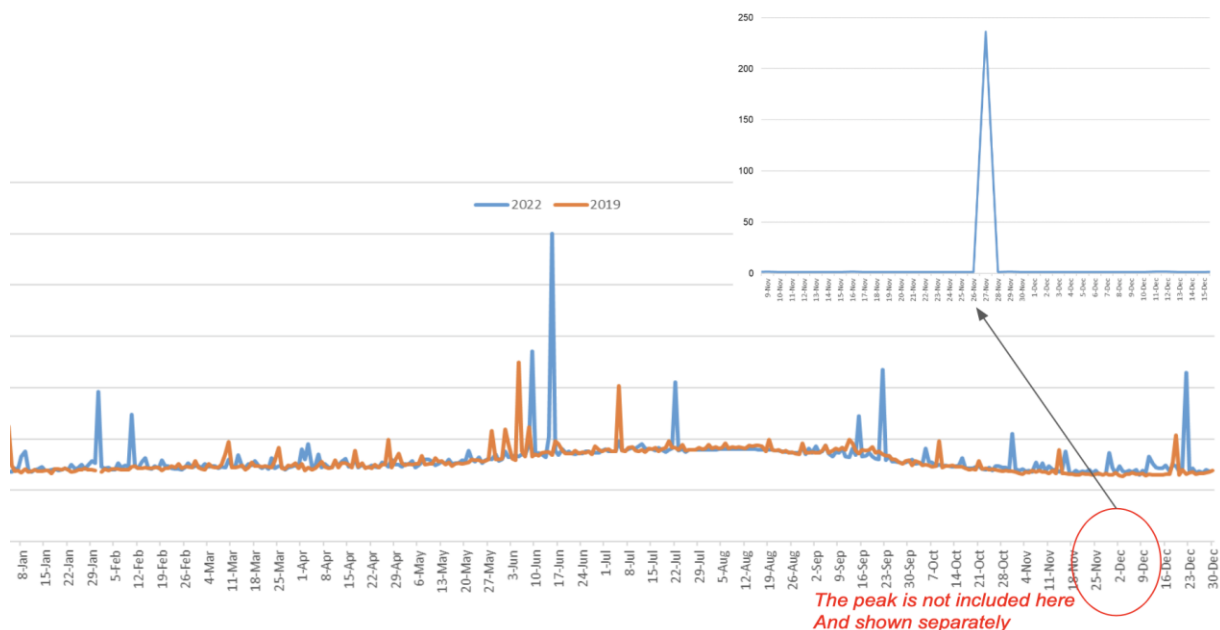


Figure 2.4.7 Time series of daily CH₄ emissions from the IFS2019 and 2020 inversions.

Image for 28-Nov-2022 - day with very high emissions

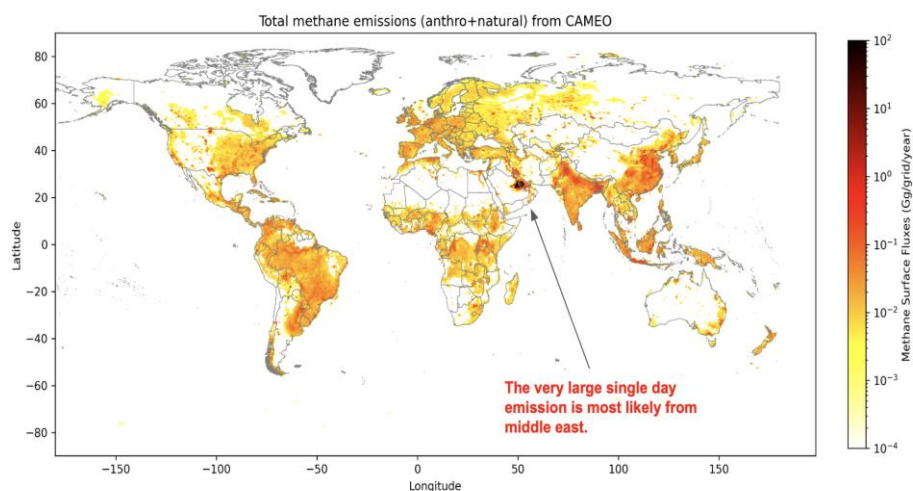


Figure 2.4.8 Global distribution of CH₄ IFS posterior emissions on 28 Nov 2022 which is a global spike of emissions on that specific day.

We show in Figure 2.4.8 the map of emissions on 28 Nov 2022 which is a spike of emissions separately illustrated in Figure 2.4.7. It seems that the spike originates from very high emissions being highly localized in Saudi Arabia and Qatar. The reasons for it need to be investigated with the IFS inversion team. We further show in Figure 2.4.9 the temporal distribution of spikes from three other regions and it can be seen that the largest spikes of the IFS inversion are found in China, with smaller but detectable additional spikes in USA and Europe during specific days of the year 2019.

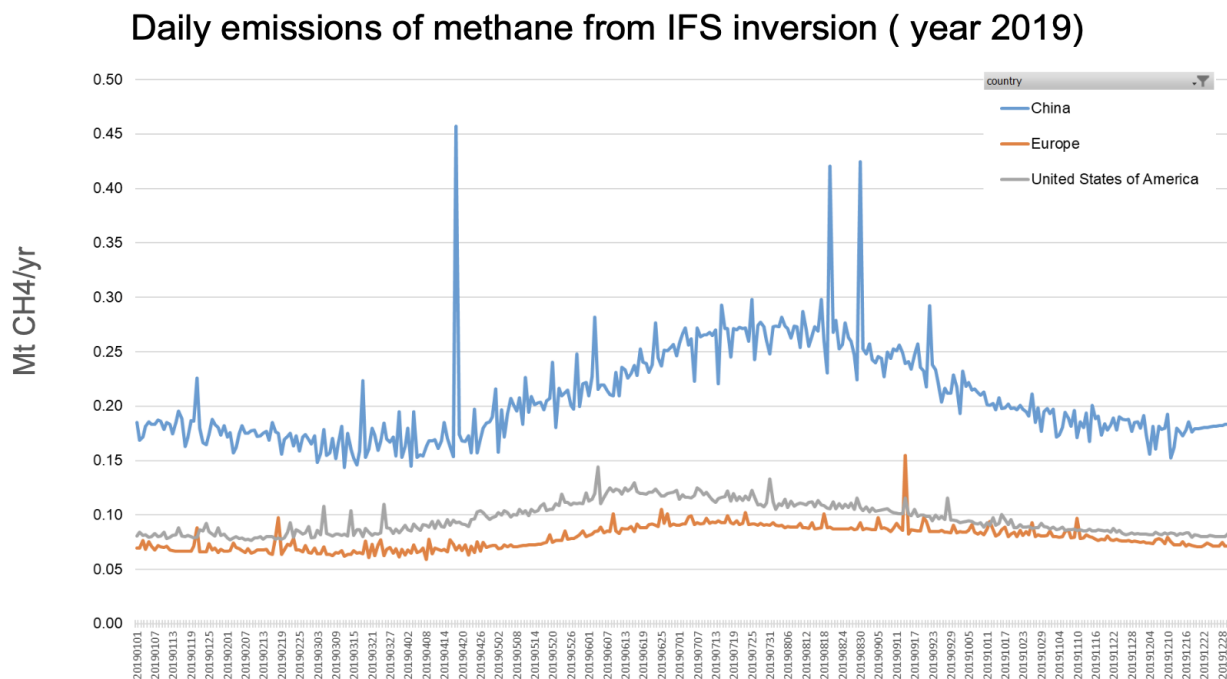


Figure 2.4.9 the temporal distribution of CH_4 emissions for the IFS 2019 inversion in three regions

Finally, Figure 2.4.10 displays total emissions from the IFS inversion in the year 2019 compared with the basin-scale high resolution inversions obtained from individual TROPOMI images (see section 2.4.2 and Fig 2.4.3). We see globally consistent values across the different basins, but IFS significantly overestimates emissions in Shanxi (coal) and South Africa (coal), and underestimates emissions in USA basins of Anardako (mixed oil and gas), Appalachian (mixed oil, coal and gas), Iraq (oil and gas) and Turkmenistan, two basins where most emissions come from ultra emitters. This result suggests that gas emissions from ultra emitters detected by the TROPOMI satellite are not captured by the IFS2019 inversion, possibly because of its spatial resolution being too coarse to identify sporadic large but highly localised gas leaks from ultra emitters.

CAMEO

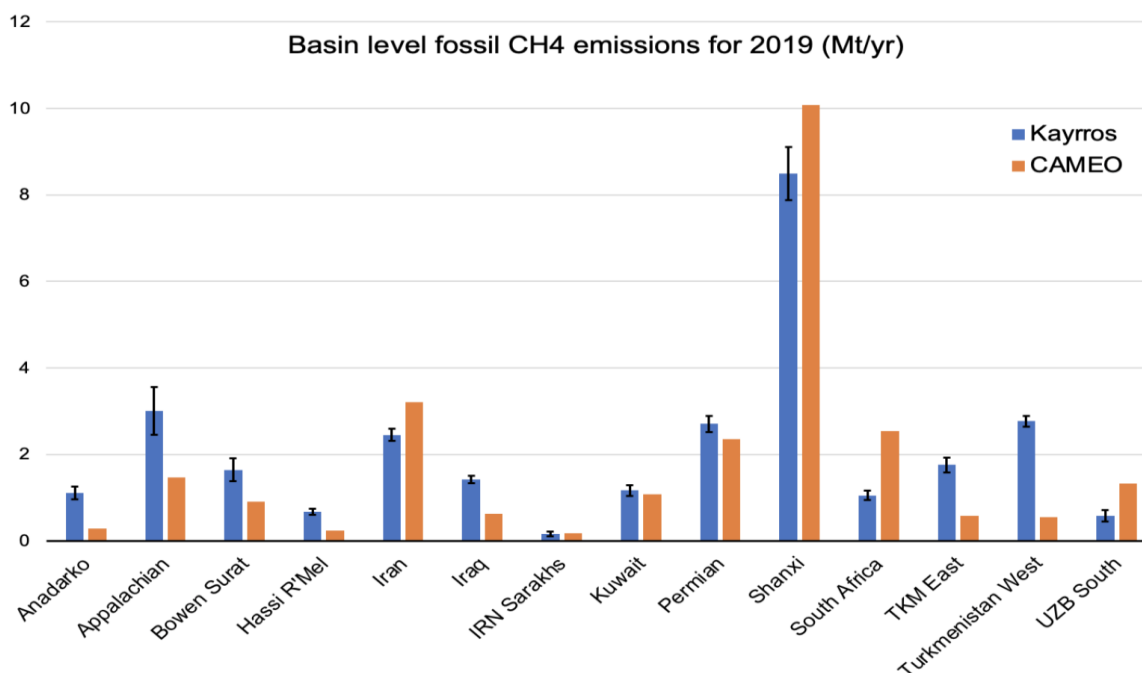


Figure 2.4.10 Comparison of CAMEO CH₄ IFS inversion over selected basins with regional high-resolution inversions per basins obtained from TROPOM images

2.5 Evaluation of NO_x inversions

We have evaluated the NO_x emissions of the IFS CAMEO inversion, which are derived by assimilation in the ECMWF IFS-COMPO Cy48R1 system, by comparing them with other NO_x emission datasets: NO_x emissions derived with the DECSO algorithm using TROPOMI observations, the emissions of CAMS, and the reported emissions to the EEA for Europe.

2.5.1 Inversion algorithms of NO_x

DECSO algorithm

The inversion algorithm DECSO (Daily Emissions Constrained by Satellite Observations) has been developed at KNMI for the purpose of deriving emissions for short-lived gases (Mijling and van der A, 2012). DECSO is using a Kalman Filter implementation for optimizing emissions. The emission forecast model is based on persistency from the analysis, while the concentrations are calculated from the emissions by a chemical transport model (CTM) and compared to satellite observations. The sensitivity of concentrations to emissions is calculated from multiple forward trajectories to account for the transport of the short-lived gas, but only a single CTM forward run is needed. Recent developments of the algorithm to improve its resolution and quality have led to the release of version 6.4. The most important recent updates are the use of a recent version of the CTM, improved use of TROPOMI observations and changes in the sensitivity matrix calculations.

The CTM in DECSO has been upgraded to the latest version of the Eulerian regional off-line CTM CHIMERE v2020r3 (Menuet et al., 2021). The implementation of CHIMERE in DECSO was described in Ding et al. (2017). CHIMERE is combined with the Copernicus Landcover 2019 data (Buchhorn et al., 2020) and HTAP v3 (Hemispheric Transport of Air Pollution, Crippa et al., 2023) of 2018 for the source sector split of the emissions. The meteorological

CAMEO

input data for CHIMERE are the operational European Centre for Medium-Range Weather Forecasts (ECMWF) weather forecasts.

The error parametrizations for the emission model and observations are based on the Observation-minus-Forecast (OmF) and the Observation-minus-Analysis (OmA) statistics of previous runs. The latest version of DECSO can be applied to simultaneous optimisation of emissions of NO_x and NH₃ (Ding et al., 2024).

Although HTAP v3 has been used for the sector distribution of NO_x emissions and the other species in CHIMERE, no use is made of a-priori (bottom-up) emissions in DECSO. DECSO is using a persistency forward model in which the emissions of the current day are equal to the emissions of the previous day. In addition, there is a strong dependency of the calculated emissions on the observations as shown in Ding et al. (2020). Since the derived emissions are updated by addition and not by multiplication factors, unknown sources or emission changes are detected fast.

In a post-processing step, the total monthly NO_x emissions are split into anthropogenic and (biogenic) soil emission contributions. The soil emissions show a strong seasonal cycle with low emissions in winter, while the anthropogenic emissions are more constant over the year. The soil NO_x emissions are derived by fitting the monthly emissions in a selection of grid-cells without any significant anthropogenic contribution according to land-use data. In this way the monthly averaged soil NO_x emissions in the categories for forest, agricultural and shrub-land are derived. These monthly soil NO_x emissions are weighted with the land-use type of these 3 categories in each grid cell and subtracted from the total derived NO_x emissions to end up with the anthropogenic NO_x emissions discussed in this study. This splitting method is described in detail in Lin et al. (2024).

For the monthly emissions also the precision of the emission in each grid cell has been calculated. Each daily NO_x emission per grid cell derived by DECSO is accompanied by a standard deviation calculated according to the Kalman Filter equations (the standard deviation is part of the emission data product of DECSO). Since the daily emission calculation in DECSO uses the emissions of the previous day as the starting point, the resulting emissions will show an autocorrelation in their errors. For each grid cell the autocorrelation function ρ_k (for time lag k) has been calculated for each month. We see typically that the autocorrelation effects in the errors have disappeared completely after about 1 week.

When calculating the variance of the monthly mean values, we must take this autocorrelation function into account. The variance S of the monthly mean NO_x emissions per grid cell is calculated following Box et al. (2008) as

$$S = \frac{\sigma^2}{n} \left[1 + 2 \sum_{k=1}^{n-1} \left(1 - \frac{k}{n} \right) \rho_k \right],$$

where σ is the mean standard deviation of the emissions over the month and n is the number of days in the month. We assume here that σ is not varying a lot over the month. This precision σ is calculated in the Kalman equations of the inverse modelling and it depends on the precision of the TROPOMI NO₂ superobservations. The precision depends on the location and emission magnitude, but on average the precision is estimated as 8% for annual emissions, 25% for monthly emissions and between 10 and 60 % for daily emissions.

DECSO has been applied to many regions in the world (Europe, Northern hemispheric Africa, part of South America, the Middle East, India, East China), usually using a spatial resolution of 0.2° x 0.2°. More detailed information on the method and recent updates can be found in Van der A et al. (2024), Ding et al. (2024) and Lin et al. (2024).

CAMEO

Satellite data

The NO_x inversions are based on NO₂ observations of TROPOMI onboard the Sentinel 5P satellite, which was launched in October 2017 and is flying a sun-synchronous polar orbit with a local overpass time of 13:30. The measured NO₂ tropospheric columns have a spatial resolution of 5.5 x 7 km (5.5 x 3.5 km since 6 August 2019) in nadir. We are using the latest version 2.4 reprocessed and offline TROPOMI NO₂ observations (van Geffen et al, 2022) converted to super-observations as described in Ding et al. (2020). To avoid the influence of NO₂ in the free troposphere, governed by processes like lightning, deep convection, aircraft emissions or long-range transport, we adapted the TROPOMI NO₂ retrieval by calculating a partial column up to the 700 hPa level instead of the tropopause level. The stratosphere + free troposphere NO₂ column from the TM5-MP (Tracer Model 5, <https://tm5.site.pro/>, Williams et al., 2017) assimilation system are now subtracted from the satellite-observed total column, and new retrieved layer column amounts, air-mass factors and kernels are computed for the surface to 700 hPa layer in the same way as they are computed for the tropospheric column (van Geffen et al., 2022). The observations with a cloud radiance fraction of more than 50% (this corresponds to a cloud fraction of about 20%) have not been used. For Europe, it means that about 45% of the observations are used.

IFS-COMPO

The CAMEO emissions have been provided at 0.1° x 0.1° resolution. The inversion itself is performed using the ECMWF IFS-COMPO Cy48R1 system at about 80 x 80 km resolution, while the forward model is run at about 25 km. A spatial error correlation length scale of 100 km has been used in the inversion. For the prior emission uncertainty, the standard deviation is 50% and the correlation length is 300 km.

Recent model and data assimilation innovations of the CAMS system implemented in the Cy48R1 upgrade of 2023 as well as a list of emission datasets used are discussed in Eskes et al. (2024). and in section 2.3.2.

For these comparison the CAMEO emissions are binned to 0.2° x 0.2°, the same resolution as DECSO.

2.5.2 Emission data for evaluation

European reported emissions (LRTAP and NEC and E-PRTR)

For comparison of the emission results in Europe, we will use several inventories, often based on official emissions reported to the European Environmental Agency (EEA). The first one is the inventory of national emissions per source category reported under the National Emission reductions Commitments (NEC) Directive of the European Union. Another similar inventory is the Emission inventory reported under the Convention on Long-range Transboundary Air Pollution (LRTAP), which gives the country totals of emissions in various source categories. The last one we will use is the European Pollutant Release and Transfer Register (EPRTTR, 2012), which is a database of the individual emissions of the biggest industrial facilities (above 0.1Mg/year) in Europe. The E-PRTR emissions data are reported on an annual basis. From here on we will call those databases simply NEC, LRTAP and E-PRTR.

CAMS-GLOB-TEMPO

Besides comparison with DECSO and the reported European emissions, we will also compare the IFS emissions to the global anthropogenic emission inventory CAMS-GLOB-ANT version

CAMEO

5.3 (Soulie et al., 2023) combined with temporal profiles (CAMS-GLOB-TEMPO) as described in Guevara et al. (2021). These Copernicus Atmospheric Monitoring Service (CAMS) global emissions are hereafter called CAMS-GLOB. For these monthly CAMS-GLOB emissions, we use the total emissions rebinned from $0.1^\circ \times 0.1^\circ$ to $0.2^\circ \times 0.2^\circ$ and exclude the soil emissions (i.e. agricultural categories), since soil emissions are also excluded in DECSO and in IFS-COMPO Cy48R1.

CAMS-REG

For the European domain we will use the regional anthropogenic emission inventory CAMS-REG-ANT v5.1 for air quality in Europe (Kuenen et al., 2022) developed for the Copernicus Atmospheric Monitoring Service (CAMS), hereafter called CAMS-REG. For these monthly CAMS-REG emissions we use the total emissions regridded from $0.1^\circ \times 0.05^\circ$ to $0.2^\circ \times 0.2^\circ$ and exclude the soil emissions (i.e. agricultural categories).

2.5.3 Results for NO_x emissions

Country totals

For a part of the European domain, we have calculated the country totals of anthropogenic NO_x for CAMEO, DECSO, CAMS-REG, and compared these to the reported emissions of LRTAP and NEC. Note that the country totals of CAMS-REG and CAMS-GLOB are almost equal, therefore, we show only CAMS-REG here. In Figure 2.5.1, the results are shown for the year 2019. We see that CAMEO has in general somewhat higher total emissions, which is caused by the CAMEO summer emissions. The a-priori emissions of CAMEO are very similar to CAMS-REG, but during the summer months the CAMEO emission analysis becomes much higher (compared to emission in the beginning of the year), while slightly reducing with respect to the summer emissions towards the end of the year.

In the next sections we will further study the spatial and temporal distribution of the emissions.

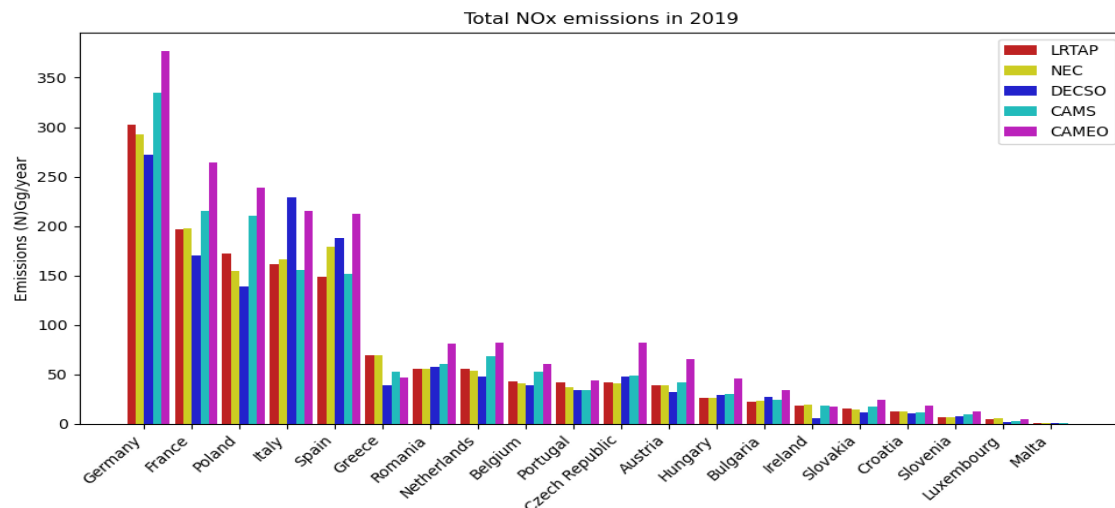


Figure 2.5.1 Country totals of anthropogenic NO_x emissions as provided by various inventories or inversion datasets. Note that Ireland is not completely included in the study domain for this comparison, therefore DECSO, CAMS-REG and CAMEO are too low for this country.

Spatial distribution

First a comparison is made for the distribution of emissions in 2019 for a large part of Europe on the resolution of DECSO, i.e. 0.2° by 0.2° . CAMS-REG has been rescaled to the same

CAMEO

resolution for this comparison. Figure 2.5.2 shows six panels with the distribution for DECSO, CAMEO and CAMS-REG, the absolute and relative difference between DECSO and CAMEO, and the absolute difference between CAMS-REG and CAMEO. From these images we can conclude that CAMEO has lower emissions over cities, where the emissions seem to be spread over a larger area. Both CAMS-REG and DECSO have sharper defined hotspots for cities or industry. The rural regions on the other hand are higher in the emissions of CAMEO. The emissions from ship tracks of CAMEO are in between those of DECSO and CAMS-REG. A few emission hotspots are visible in CAMEO (notably in Romania, Turkey, and Algeria), which do not exist in both CAMS-REG and DECSO. An example of such an emissions source is shown in Figure 2.5.3., which shows the comparison for the coast of Algiers between Oran and Algiers. The biggest source of CAMEO is centered over the Sea near the coast. Neither DECSO nor the CAMS-REG database show an emission hotspot at this location. The source is puzzling, since it already exists on 1 January 2019 the CAMEO run and it is hardly adapted during 2019. Also, the CAMS-GLOB database does not show this source.

An example to show the smoothing of the emissions over cities is presented in Figure 2.5.4, which shows the emissions over Berlin as derived by DECSO, CAMEO and CAMS-REG. It reflects the lower resolution of the CAMEO emissions. We also see that the rural emissions further away from Berlin are higher than the other inventories.

For completeness, we show the difference between DECSO and CAMEO for the regions East China (figure 2.5.5), Middle East (Figure 2.5.6) and part of North Africa (Figure 2.5.7). For these regions we can draw the same conclusions as for the comparison over Europe.

CAMEO

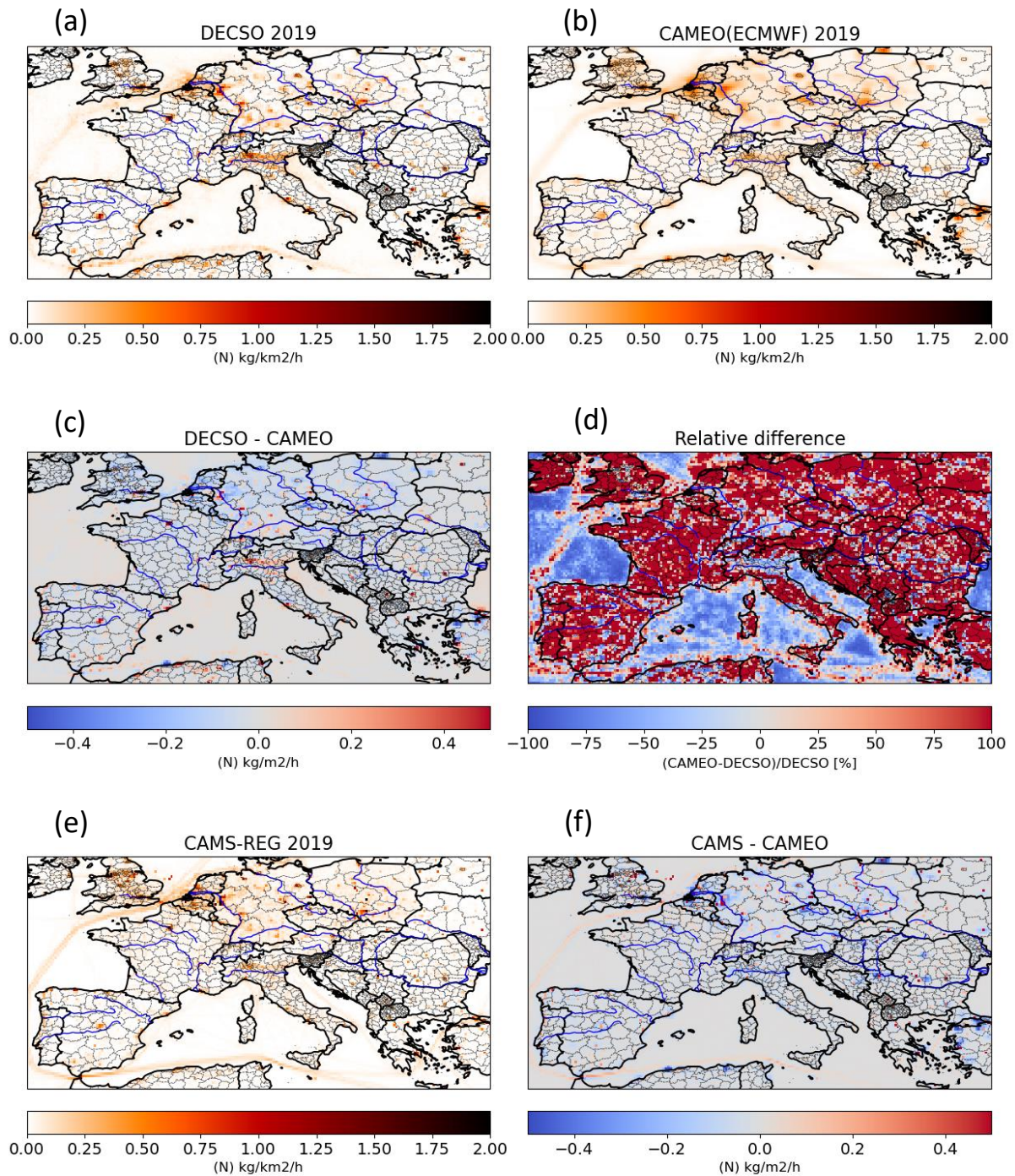


Figure 2.5.2 Comparison of the average European NO_x emissions for 2019 of (a) DECSO, (b) CAMEO-ECMWF. In subfigure (c) the absolute differences between DECSO and CAMEO are shown. In subfigure (d) the relative differences between DECSO and CAMEO are shown. Subfigure (e) shows the NO_x emissions of CAMS-REG and (f) the absolute differences between CAMS-REG and CAMEO.

CAMEO

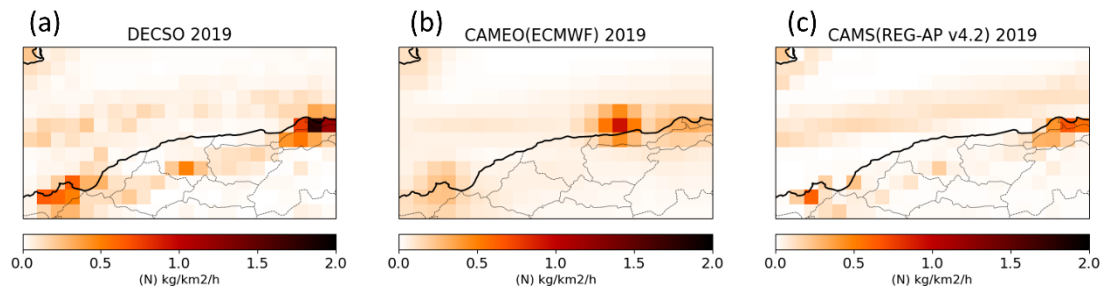


Figure 2.5.3 Average NO_x emissions as derived using DECSO vs. using CAMEO-ECMWF and CAMS-REG. The region shows the Northern African coast of Algeria between the cities of Oran at the left and Algiers at the right.

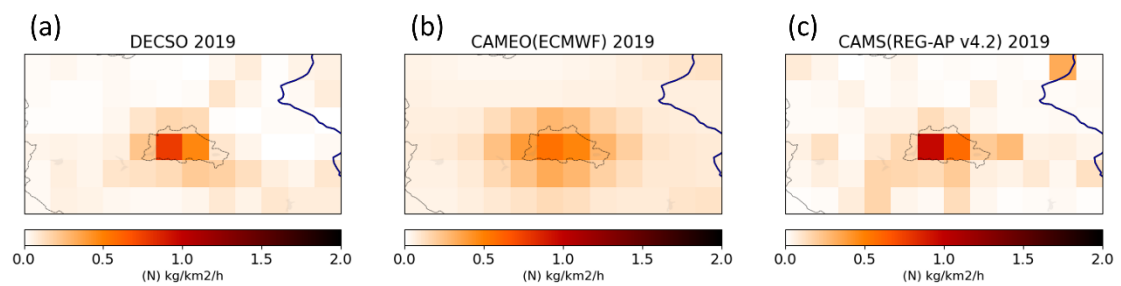


Figure 2.5.4 Comparison of the average NO_x emissions over Berlin in 2019 of (a) DECSO, (b) CAMEO-ECMWF, (c) CAMS-REG. The grid cells are 0.2° x 0.2°

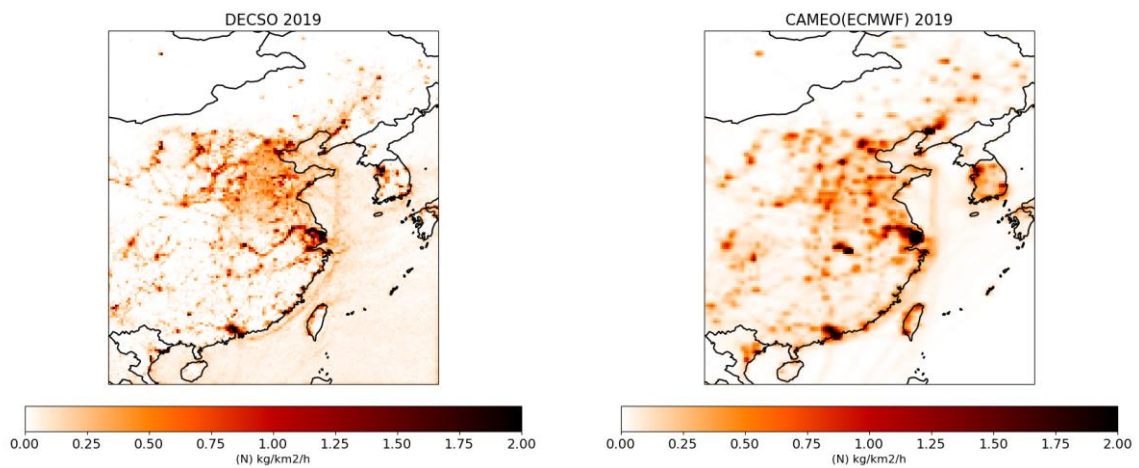


Figure 2.5.5 Comparison of the average NO_x emissions over East China in 2019 of DECSO (left panel) and CAMEO (right panel).

CAMEO

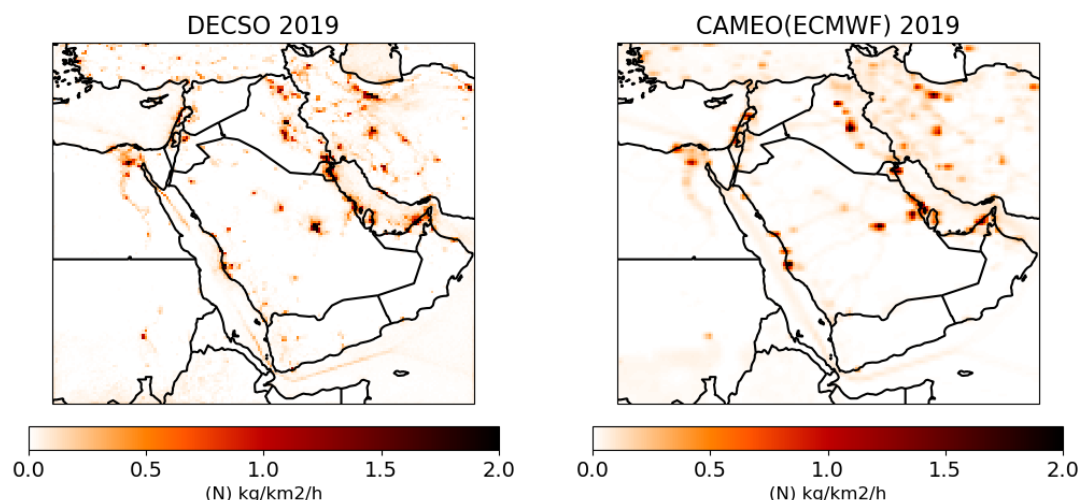


Figure 2.5.6 Comparison of the average NO_x emissions over the Middle East in 2019 of DECSO (left panel) and CAMEO (right panel).

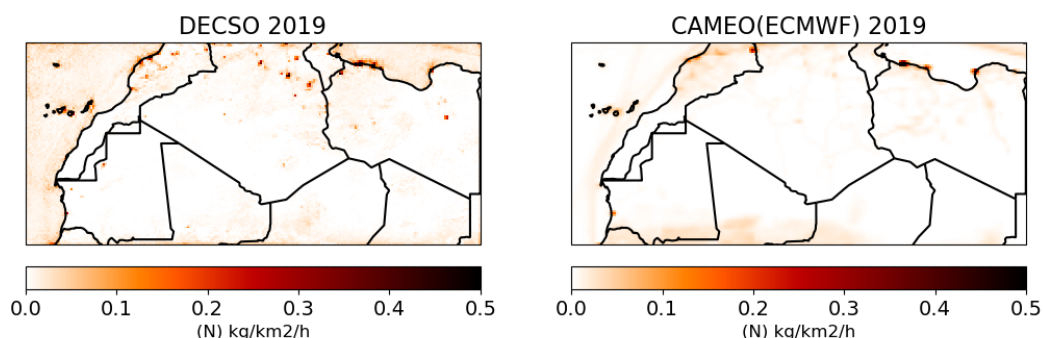


Figure 2.5.7 Comparison of the average NO_x emissions over Northern Africa in 2019 of DECSO (left panel) and CAMEO (right panel).

Daily emission updates

We further checked the daily updates (i.e. posterior emissions minus prior emissions) of CAMEO. We calculated the average daily updates for each month in the year 2019. In Figure 2.5.8, we see the results for the month June and in Figure 2.5.9 for the month December. Positive updates are dominating throughout the year, which means that an overall increase in emissions is visible over the year 2019. Over sea no adjustments are seen, and apparently shipping emissions are not adjusted in the CAMEO system. The updates of the emissions in the summer months are in general positive and with a stronger magnitude than the winter months as shown in the Figure 2.5.8 and 2.5.9. The relative updates show smooth patterns over large regions. To investigate this further we looked at the daily relative update for 15 October (randomly chosen) shown in Figure 2.5.10. The patterns of the changes are slowly changing over hundreds of kilometers, which may be caused by the long correlation length of the error covariances used in the IFS system. For comparison, we show the update of DECSO over Europe on the same day in Figure 2.5.11. DECSO has a correlation length of 10 km for the observation error covariances and of 0.5 km for the emission error covariances. In DECSO the emission adjustments have fine-scale features, with positive and negative adjustments in nearby cells, demonstrating that TROPOMI is providing local emission information at the 0.2 degree grid cell size (or better). The noise over the Mediterranean or Atlantic reflects the shipping signals which differ strongly from one day to the next. These fine-scale adjustments are in contrast with the spatially smooth CAMEO relative adjustments.

CAMEO

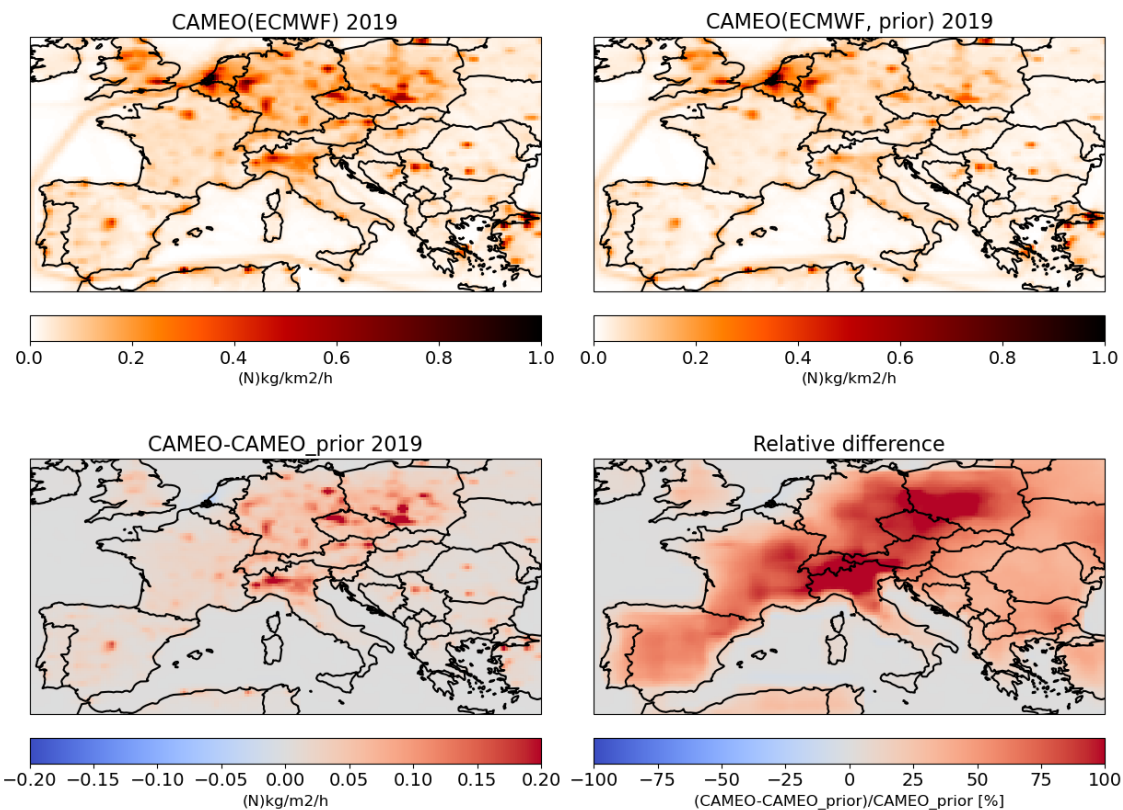


Figure 2.5.8 Average daily updates of the NO_x emissions of the IFS system for the month June 2019.

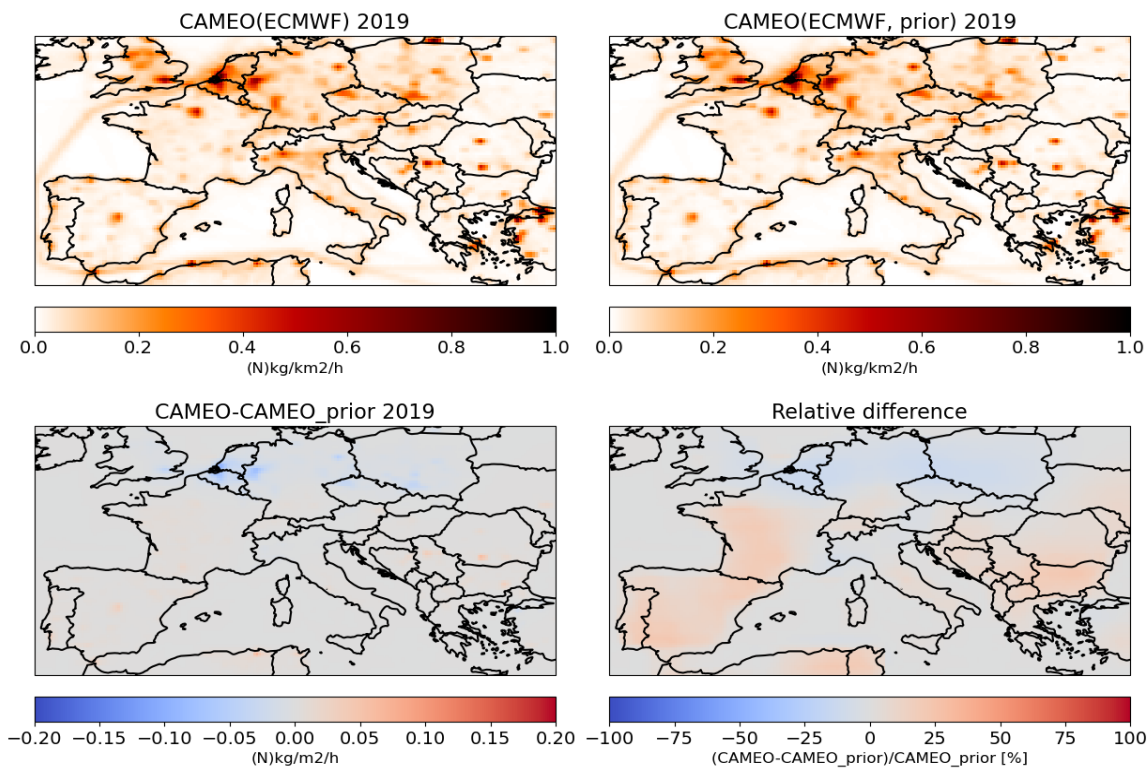


Figure 2.5.9 Average daily updates of the NO_x emissions of the IFS system for the month December 2019.

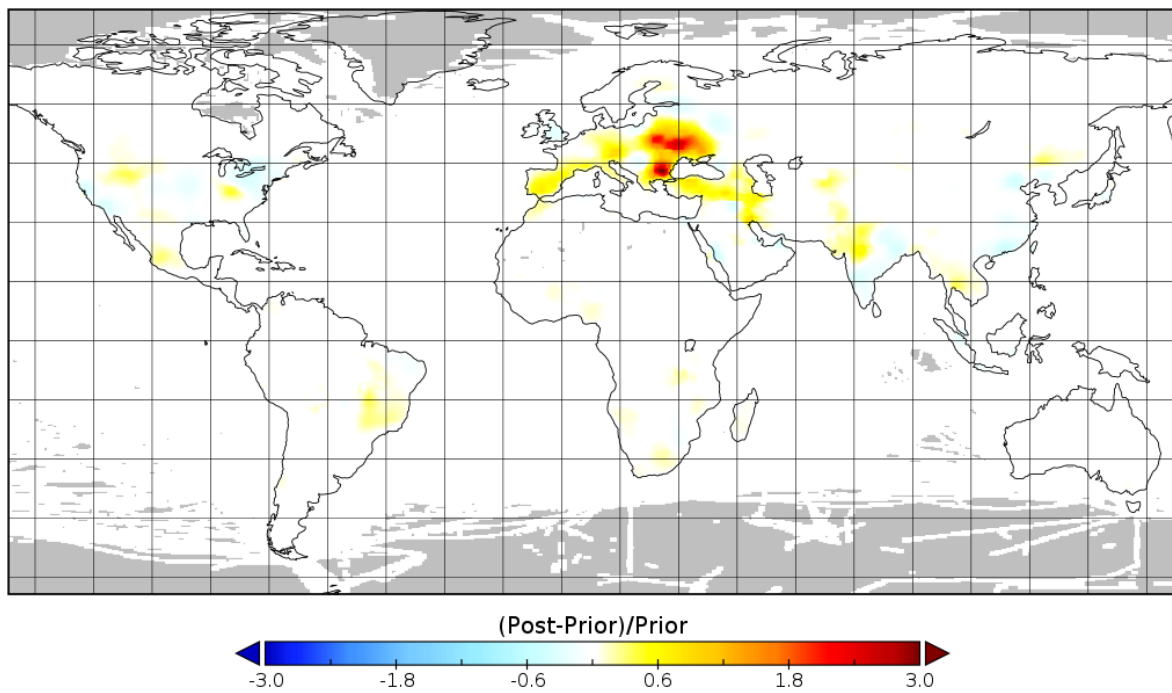


Figure 2.5.10 Relative change of NOx priori emissions to the NOx posteriori emissions of the IFS system for 15 October 2019.

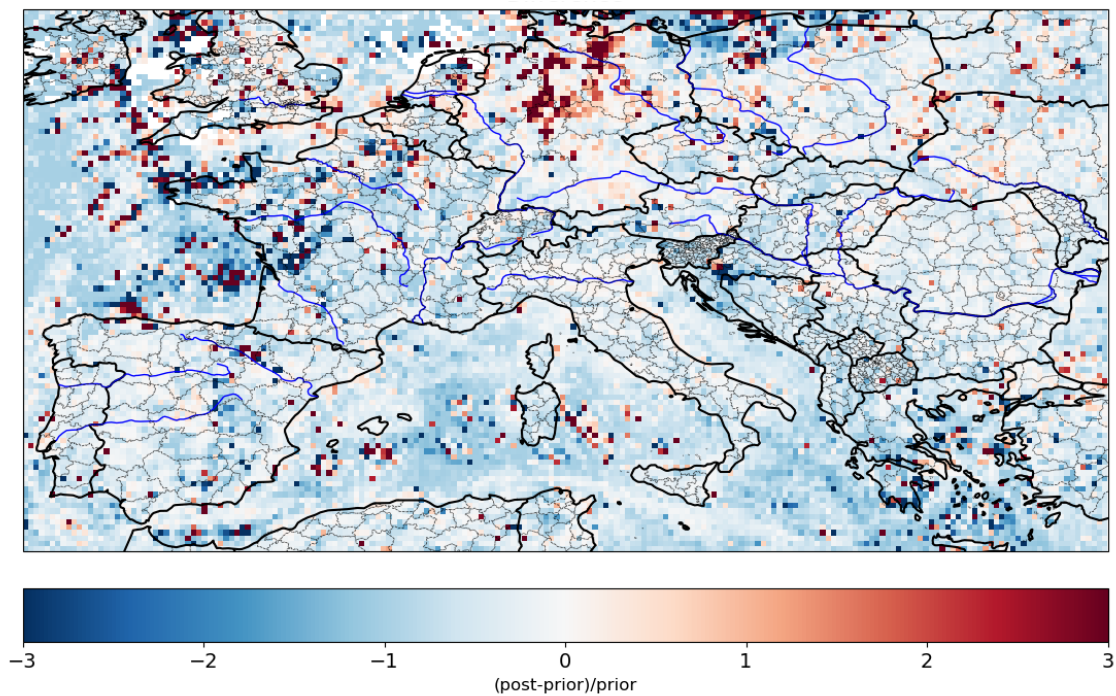


Figure 2.5.10 Relative change of NOx priori emissions to the NOx posteriori emissions of the DECSO system for 15 October 2019.

Cities and industrial hotspots

A selection of big cities and isolated industrial hotspots are selected for comparison of the magnitude of emissions in 2019. To compensate for the different intrinsic resolution, we apply the comparison on the totals of 3 by 3 grid cells (about 40 x 60 km) centred around the city or industry. Figure 2.5.11 shows the results for European cities and for four thermal power plants, while Figure 2.5.12 displays the results for selected cities in Europe, East Asia, Middle East and North Africa. We see a reasonable agreement in these Figures between the two inventories. DECSO has higher emissions (about 20% on average) in most cities, maybe because the emissions in CAMEO are spread further than 3 by 3 grid cells.

Temporal evaluation of industrial sources

To check the temporal evolution of the emissions, four big power plants in Europe are selected that are isolated from other big sources of NO_x: the Maritsa complex in Bulgaria, Belchatow power plant in Poland, Sostanj power plant in Slovenia, and the Amyntheon power plants in Greece. Their monthly emissions are shown in Figure 2.5.13 for CAMEO, CAMS-REG and DECSO. The emissions reported by the E-PRTR database are also included, but these are only known as annual averages. The CAMEO emissions are often in good agreement with the DECSO and CAMS emissions. CAMS-REG shows less variability than the emissions of CAMEO and DECSO, which are both derived from satellite observations.

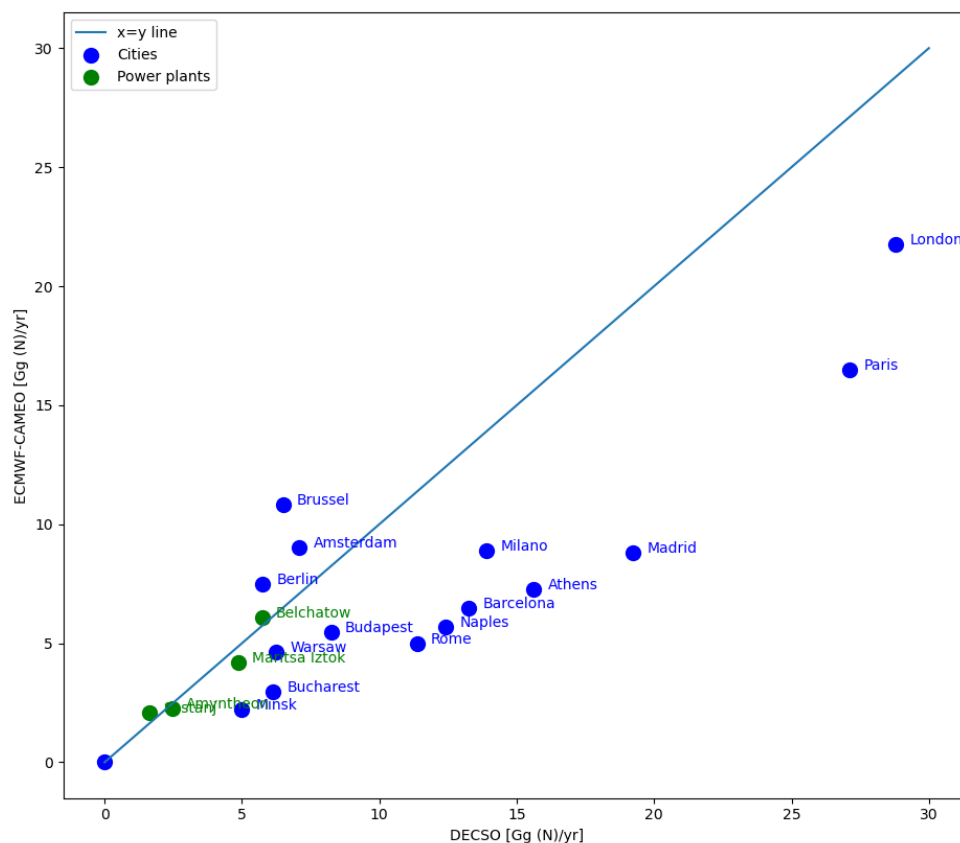


Figure 2.5.11 Average NO_x emissions per city (blue points) or power plant (green points) as derived by DECSO vs. CAMEO. Shown are results for capitals and other major cities in Europe. The green points refer to the emissions of four of the biggest coal power plants in Europe.

CAMEO

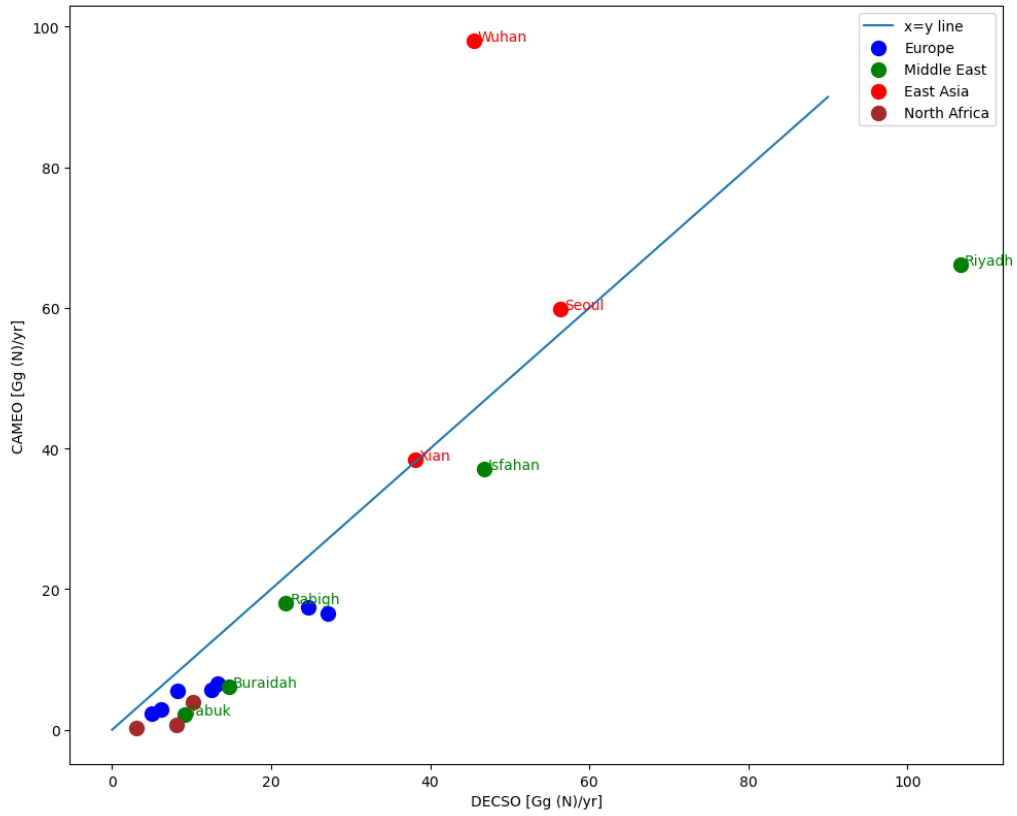


Figure 2.5.12 Average NO_x emissions per city as derived using DECSO vs. CAMEO. Results are shown for a few of the biggest cities in Europe, Middle East, East Asia and North Africa. The colors indicate the region the city belongs to.

CAMEO

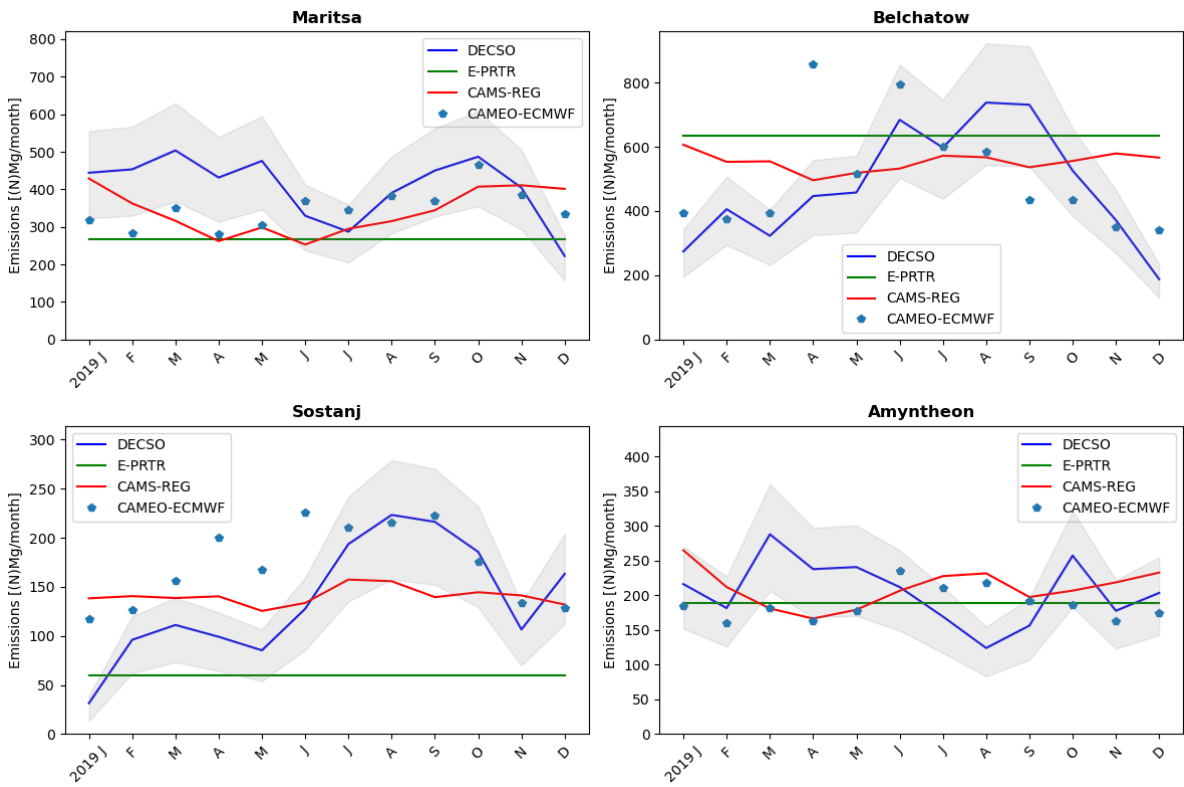


Figure 2.5.13 Time series of monthly NO_x emissions of isolated power plants as reported by DECSO (blue line), E-PRTR (green line), CAMS-REG (red line), and CAMEO-ECMWF (blue dots). The grey shadow regions show the estimated uncertainty of the DECSO emissions.

2.6 Conclusions

The CAMEO CO₂ emissions have been compared only for point sources to localized inversions based on OCO-2 and OCO-3 for \approx 300 point sources one-shot estimation during the satellite overpass. The results for CO₂ point sources show large differences between the CAMEO IFS inversion and local inversions which may be related to the prior emission inventory used by CAMEO and the relatively coarse spatial resolution of the inversion system that may lack ability to simulate short distance enhancements of XCO₂ in plumes.

The results for the CAMEO CH₄ inversion based on multimodal satellite XCH₄ observations have been compared with global inversions using GOSAT and surface stations, and with regional high resolution inversions estimates of fossil CH₄ emissions over selected extraction basins, based on TROPOMI images at their native resolution. The results present good comparison with regional budgets of other global inversions for fossil CH₄ emissions and a good comparison with high resolution emissions from 14 basins altogether comprising about 25% of global fossil CH₄ emissions. The CAMEO inversion does not seem to detect sporadic point leaks emissions. The time series of inversion results for CH₄ emissions over large regions show spikes during some days perhaps related to the short assimilation window used.

The CAMEO NO_x emissions have been compared to NO_x emissions from the DECSO algorithm based on TROPOMI NO₂ satellite observations, CAMS databases (global and regional), and several databases of reported emissions of Europe (E-PRTR, NEC, LRTAP). The comparison was performed for four different regions: Europe, East-Asia, Middle East, and North Africa. The spatial distribution has been compared from country-level to city-level. In addition, the seasonal variation of the industrial hotspots has been compared.

In general, the magnitude of CAMEO emissions for industrial sources are comparable to other inventories, but its city emissions were usually lower and rural emissions were higher. The resolution of the CAMEO emissions (80 km) was visibly lower in the maps than other inventories (10-20 km). However, the analysis increments of CAMEO showed an even lower resolution, maybe because of the long correlation length of the spatial error in the IFS system. This might also be the explanation that some strong point sources remain persistent in the CAMEO emissions but are unknown in other inventories. Emission increments are expected to vary strongly in space at fine scales as nearby sources may have uncorrelated emission errors. A system like DECSO is able to resolve this, while the current CAMEO setup cannot.

2.7 Deviations and countermeasures

No deviations have been encountered.

2.8 CAMEO Project Partners:

ECMWF	EUROPEAN CENTRE FOR MEDIUM-RANGE WEATHER FORECASTS
Met Norway	METEOROLOGISK INSTITUTT
BSC	BARCELONA SUPERCOMPUTING CENTER-CENTRO NACIONAL DE SUPERCOMPUTACION
KNMI	KONINKLIJK NEDERLANDS METEOROLOGISCH INSTITUUT-KNMI
SMHI	SVERIGES METEOROLOGISKA OCH HYDROLOGISKA INSTITUT
BIRA-IASB	INSTITUT ROYAL D'AERONOMIE SPATIALE DE BELGIQUE
HYGEOS	HYGEOS SARL
FMI	ILMATIETEEN LAITOS
DLR	DEUTSCHES ZENTRUM FUR LUFT - UND RAUMFAHRT EV
ARMINES	ASSOCIATION POUR LA RECHERCHE ET LE DEVELOPPEMENT DES METHODES ET PROCESSUS INDUSTRIELS
CNRS	CENTRE NATIONAL DE LA RECHERCHE SCIENTIFIQUE CNRS
GRASP-SAS	GENERALIZED RETRIEVAL OF ATMOSPHERE AND SURFACE PROPERTIES EN ABREGE GRASP
CU	UNIVERZITA KARLOVA
CEA	COMMISSARIAT A L ENERGIE ATOMIQUE ET AUX ENERGIES ALTERNATIVES
MF	METEO-FRANCE
TNO	NEDERLANDSE ORGANISATIE VOOR TOEGEPAST NATUURWETENSCHAPPELIJK ONDERZOEK TNO
INERIS	INSTITUT NATIONAL DE L ENVIRONNEMENT INDUSTRIEL ET DES RISQUES - INERIS
IOS-PIB	INSTYTUT OCHRONY SRODOWISKA - PANSTWOWY INSTYTUT BADAWCZY
FZJ	FORSCHUNGSZENTRUM JULICH GMBH
AU	AARHUS UNIVERSITET
ENEA	AGENZIA NAZIONALE PER LE NUOVE TECNOLOGIE, L'ENERGIA E LO SVILUPPO ECONOMICO SOSTENIBILE

2.9 References

- Alvarez, R. A., Zavala-Araiza, D., Lyon, D. R., Allen, D. T., Barkley, Z. R., Brandt, A. R., Davis, K. J., Herndon, S. C., Jacob, D. J., Karion, A., Kort, E. A., Lamb, B. K., Lauvaux, T., Maasakkers, J. D., Marchese, A. J., Omara, M., Pacala, S. W., Peischl, J., Robinson, A. L., Shepson, P. B., Sweeney, C., Townsend-Small, A., Wofsy, S. C., and Hamburg, S. P.: Assessment of methane emissions from the U.S. oil and gas supply chain, *Science* (1979), 361, 186–188, <https://doi.org/10.1126/science.aar7204>, 2018.
- Box, Jenkins, Reinsel, *Time Series Analysis: Forecasting and Control*, 4th Ed. Wiley (2008), ISBN 978-0-470-27284-8, p.30.
- Buchhorn, M. ; Smets, B. ; Bertels, L. ; De Roo, B. ; Lesiv, M. ; Tsendbazar, N. - E. ; Herold, M. ; Fritz, S, Copernicus Global Land Service: Land Cover 100m: collection 3: epoch 2019: Globe, 2020, DOI: 10.5281/zenodo.3939050
- CEDS Release Notes: <https://github.com/JGCRI/CEDS/wiki/Release-Notes>, last access: 11 May 2023.
- Chen, Z., Jacob, D. J., Gautam, R., Omara, M., Stavins, R. N., Stowe, R. C., Nesser, H., Sulprizio, M. P., Lorente, A., Varon, D. J., Lu, X., Shen, L., Qu, Z., Pendergrass, D. C., and Hancock, S.: Satellite quantification of methane emissions and oil–gas methane intensities from individual countries in the Middle East and North Africa: implications for climate action, *Atmospheric Chem. Phys.*, 23, 5945–5967, <https://doi.org/10.5194/acp-23-5945-2023>, 2023.
- Chevallier, F., B. Zheng, et al. (2020), Local anomalies in the column-averaged dry air mole fractions of carbon dioxide across the globe during the first months of the coronavirus recession, *Geophys. Res. Lett.*, [doi:10.1029/2020GL090244](https://doi.org/10.1029/2020GL090244).
- Chevallier, F., Broquet, G., Zheng, B., Ciais, P., & Eldering, A. (2022). Large CO₂ emitters as seen from satellite: Comparison to a gridded global emission inventory. *Geophysical Research Letters*, 49, e2021GL097540. <https://doi.org/10.1029/2021GL097540>
- Crippa, M., Guizzardi, D., Butler, T., Keating, T., Wu, R., Kaminski, J., Kuenen, J., Kurokawa, J., Chatani, S., Morikawa, T., Pouliot, G., Racine, J., Moran, M. D., Klimont, Z., Manseau, P. M., Mashayekhi, R., Henderson, B. H., Smith, S. J., Suchyta, H., . . . Foley, K. (2023). The HTAP_v3 emission mosaic: merging regional and global monthly emissions (2000–2018) to support air quality modelling and policies. *Earth Syst. Sci. Data*, 15(6), 2667-2694, <https://doi.org/10.5194/essd-15-2667-2023>
- Cusworth, D. H., Bloom, A. A., Ma, S., Miller, C. E., Bowman, K., Yin, Y., Maasakkers, J. D., Zhang, Y., Scarpelli, T. R., Qu, Z., Jacob, D. J., and Worden, J. R.: A Bayesian framework for deriving sector-based methane emissions from top-down fluxes, *Commun. Earth Environ.*, 2, 242, <https://doi.org/10.1038/s43247-021-00312-6>, 2021.
- Cusworth, D. H., Thorpe, A. K., Ayasse, A. K., Stepp, D., Heckler, J., Asner, G. P., Miller, C. E., Yadav, V., Chapman, J. W., Eastwood, M. L., Green, R. O., Hmiel, B., Lyon, D. R., and Duren, R. M.: Strong methane point sources contribute a disproportionate fraction of total emissions across multiple basins in the United States, *Proc. Natl. Acad. Sci.*, 119, e2202338119, <https://doi.org/10.1073/pnas.2202338119>, 2022.
- Deng, Z., Ciais, P., Tzompa-Sosa, Z. A., Saunio, M., Qiu, C., Tan, C., Sun, T., Ke, P., Cui, Y., Tanaka, K., Lin, X., Thompson, R. L., Tian, H., Yao, Y., Huang, Y., Lauerwald, R., Jain, A. K., Xu, X., Bastos, A., Sitch, S., Palmer, P. I., Lauvaux, T., d'Aspremont, A., Giron, C., Benoit, A., Poulter, B., Chang, J., Petrescu, A. M. R., Davis, S. J., Liu, Z., Grassi, G., Albergel, C., Tubiello, F. N., Perugini, L., Peters, W., and Chevallier, F.: Comparing national greenhouse gas budgets reported in UNFCCC inventories against atmospheric inversions, *Earth Syst Sci Data*, 14, 1639–1675, <https://doi.org/10.5194/essd-14-1639-2022>, 2022.

CAMEO

Ding, J., R.J. van der A, B. Mijling and P.F. Levelt, Space-based NO_x emission estimates over remote regions improved in DECSO, *Atmospheric Measurement Techniques*, 2017, 10, 925–938, doi:10.5194/amt-10-925-2017.

Ding, J., van der A, R. J., Eskes, H. J., Mijling, B., Stavrou, T., van Geffen, J. H. G. M., Veefkind, J.P., NO_x emissions reduction and rebound in China due to the COVID-19 crisis, *Geophysical Research Letters*, 46, e2020GL089912, <https://doi.org/10.1029/2020GL089912>, 2020.

Ding, J., van der A, R., Eskes, H., Damers, E., Shephard, M., Wichink Kruit, R., Guevara, M., and Tarrason, L.: Ammonia emission estimates using CrIS satellite observations over Europe, *Atmos. Chem. Phys.*, 24, 10583–10599, <https://doi.org/10.5194/acp-24-10583-2024>, 2024.

EDGAR v6.0 Greenhouse Gas Emissions. European Commission, Joint Research Centre (JRC) [Dataset]: <https://data.jrc.ec.europa.eu/dataset/97a67d67-c62e-4826-b873-9d972c4f670b>, last access: 11 May 2023.

EPRTTR: European Pollutant Transfer Register, database version v4.2, available at: <http://prtr.ec.europa.eu/> (last access: 5 September 2023), 2012.

Elvidge, C., Zhizhin, M., Baugh, K., Hsu, F.-C., and Ghosh, T.: Methods for Global Survey of Natural Gas Flaring from Visible Infrared Imaging Radiometer Suite Data, *Energies* (Basel), 9, 14, <https://doi.org/10.3390/en9010014>, 2015.

Eskes, H., Tsikerdeakis, A., Ades, M., Alexe, M., Benedictow, A. C., Bennouna, Y., Blake, L., Bouarar, I., Chabrillat, S., Engelen, R., Errera, Q., Flemming, J., Garrigues, S., Griesfeller, J., Huijnen, V., Ilić, L., Inness, A., Kapsomenakis, J., Kipling, Z., Langerock, B., Mortier, A., Parrington, M., Pison, I., Pitkanen, M., Remy, S., Richter, A., Schoenhardt, A., Schulz, M., Thouret, V., Warneke, T., Zerefos, C., and Peuch, V.-H.: Technical note: Evaluation of the Copernicus Atmosphere Monitoring Service Cy48R1 upgrade of June 2023, *Atmos. Chem. Phys.*, 24, 9475–9514, <https://doi.org/10.5194/acp-24-9475-2024>, 2024.

Gao, M., Xing, Z., Vollrath, C., Hugenholtz, C. H., and Barchyn, T. E.: Global observational coverage of onshore oil and gas methane sources with TROPOMI, *Sci. Rep.*, 13, 16759, <https://doi.org/10.1038/s41598-023-41914-8>, 2023.

Guevara, M., Jorba, O., Tena, C., Denier van der Gon, H., Kuenen, J., Elguindi, N., Darras, S., Granier, C., and Pérez García-Pando, C.: Copernicus Atmosphere Monitoring Service TEMPO profiles (CAMS-TEMPO): global and European emission temporal profile maps for atmospheric chemistry modelling, *Earth Syst. Sci. Data*, 13, 367–404, <https://doi.org/10.5194/essd-13-367-2021>, 2021.

Hoesly, R. M., Smith, S. J., Feng, L., Klimont, Z., Janssens-Maenhout, G., Pitkanen, T., Seibert, J. J., Vu, L., Andres, R. J., Bolt, R. M., Bond, T. C., Dawidowski, L., Kholod, N., Kurokawa, J., Li, M., Liu, L., Lu, Z., Moura, M. C. P., O'Rourke, P. R., and Zhang, Q.: Historical (1750–2014) anthropogenic emissions of reactive gases and aerosols from the Community Emissions Data System (CEDS), *Geosci Model Dev*, 11, 369–408, <https://doi.org/10.5194/gmd-11-369-2018>, 2018.

Höglund-Isaksson, L., Gómez-Sanabria, A., Klimont, Z., Rafaj, P., and Schöpp, W.: Technical potentials and costs for reducing global anthropogenic methane emissions in the 2050 timeframe –results from the GAINS model, *Environ Res Commun*, 2, 025004, <https://doi.org/10.1088/2515-7620/ab7457>, 2020.

Höglund-Isaksson, L.: Bottom-up simulations of methane and ethane emissions from global oil and gas systems 1980 to 2012, *Environmental Research Letters*, 12, 024007, <https://doi.org/10.1088/1748-9326/aa583e>, 2017.

CAMEO

Höglund-Isaksson, L.: Global anthropogenic methane emissions 2005–2030: technical mitigation potentials and costs, *Atmos Chem Phys*, 12, 9079–9096, <https://doi.org/10.5194/acp-12-9079-2012>, 2012.

Huang, K., Fu, J. S., Prikhodko, V. Y., Storey, J. M., Romanov, A., Hodson, E. L., Cresko, J., Morozova, I., Ignatieva, Y., and Cabaniss, J.: Russian anthropogenic black carbon: Emission reconstruction and Arctic black carbon simulation, *Journal of Geophysical Research: Atmospheres*, 120, <https://doi.org/10.1002/2015JD023358>, 2015.

International Energy Agency. Database documentation, Greenhouse Gas Emissions from Energy 2022 Edition. https://iea.blob.core.windows.net/assets/78ca213f-171e-40ed-bf7e-c053d4376e79/WORLD_GHG_Documentation.pdf (2022).

International Energy Agency. Global Methane Tracker Documentation 2022 Version. (2022).

International Energy Agency. Greenhouse Gas Emissions from Energy. IEA <https://www.iea.org/data-and-statistics/data-product/greenhouse-gas-emissions-from-energy> (2020).

International Energy Agency. IEA Data and statistics. IEA <https://www.iea.org/data-and-statistics/data-sets> (2021).

Janssens-Maenhout, G., Crippa, M., Guizzardi, D., Muntean, M., Schaaf, E., Dentener, F., Bergamaschi, P., Pagliari, V., Olivier, J. G. J., Peters, J. A. H. W., van Aardenne, J. A., Monni, S., Doering, U., Petrescu, A. M. R., Solazzo, E., and Oreggioni, G. D.: EDGAR v4.3.2 Global Atlas of the three major greenhouse gas emissions for the period 1970–2012, *Earth Syst Sci Data*, 11, 959–1002, <https://doi.org/10.5194/essd-11-959-2019>, 2019.

Klein Goldewijk, K., Beusen, A., Doelman, J., and Stehfest, E.: Anthropogenic land use estimates for the Holocene – HYDE 3.2, *Earth Syst Sci Data*, 9, 927–953, <https://doi.org/10.5194/essd-9-927-2017>, 2017.

Kuenen, J., Dellaert, S., Visschedijk, A., Jalkanen, J.-P., Super, I., and Denier van der Gon, H.: CAMS-REG-v4: a state-of-the-art high-resolution European emission inventory for air quality modelling, *Earth Syst. Sci. Data*, 14, 491–515, <https://doi.org/10.5194/essd-14-491-2022>, 2022.

Lauvaux, T., Giron, C., Mazzolini, M., d’Aspremont, A., Duren, R., Cusworth, D., Shindell, D., and Ciais, P.: Global assessment of oil and gas methane ultra-emitters, *Science* (1979), 375, 557–561, <https://doi.org/10.1126/science.abj4351>, 2022.

Lauvaux, T., Giron, C., Mazzolini, M., d’Aspremont, A., Duren, R., Cusworth, D., Shindell, D., and Ciais, P.: Global assessment of oil and gas methane ultra-emitters, *Science*, 375, 557–561, <https://doi.org/10.1126/science.abj4351>, 2022.

Lin, X., R. J. van der A, J. de Laat, V. Huijnen, B. Mijling, J. Ding, H. Eskes, J. Douros, M. Liu, X. Zhang, Z. Liu, European soil NO_x emissions derived from satellite NO₂ observations, *ESS Open Archive [preprint]*, 2024 DOI: 10.22541/essoar.170224578.81570487/v1.

Maasakkers, J. D., Jacob, D. J., Sulprizio, M. P., Scarpelli, T. R., Nesser, H., Sheng, J.-X., Zhang, Y., Hersher, M., Bloom, A. A., Bowman, K. W., Worden, J. R., Janssens-Maenhout, G., and Parker, R. J.: Global distribution of methane emissions, emission trends, and OH concentrations and trends inferred from an inversion of GOSAT satellite data for 2010–2015, *Atmos Chem Phys*, 19, 7859–7881, <https://doi.org/10.5194/acp-19-7859-2019>, 2019.

Maasakkers, J. D., Jacob, D. J., Sulprizio, M. P., Scarpelli, T. R., Nesser, H., Sheng, J., Zhang, Y., Lu, X., Bloom, A. A., Bowman, K. W., Worden, J. R., and Parker, R. J.: 2010–2015 North American methane emissions, sectoral contributions, and trends: a high-resolution inversion of GOSAT observations of atmospheric methane, *Atmos Chem Phys*, 21, 4339–4356, <https://doi.org/10.5194/acp-21-4339-2021>, 2021.

McNorton, J., Bousseres, N., Agustí-Panareda, A., Balsamo, G., Cantarello, L., Engelen, R., Huijnen, V., Inness, A., Kipling, Z., Parrington, M., and Ribas, R.: Quantification of methane emissions from hotspots and during COVID-19 using a global atmospheric inversion, *Atmos. Chem. Phys.*, 22, 5961–5981, <https://doi.org/10.5194/acp-22-5961-2022>, 2022.

Menut, L., B. Bessagnet, R. Briant, A. Cholokian, F. Couvidat, S. Mailler, R. Pennel, G. Siour, P. Tuccella, S. Turquety, and M. Valari. 2021. 'The CHIMERE v2020r1 online chemistry-transport model', *Geosci. Model Dev.*, 14: 6781-811.

Miller, S. M., Michalak, A. M., Detmers, R. G., Hasekamp, O. P., Bruhwiler, L. M. P., and Schwietzke, S.: China's coal mine methane regulations have not curbed growing emissions, *Nat Commun*, 10, 303, <https://doi.org/10.1038/s41467-018-07891-7>, 2019.

Mijling, B. and R.J. van der A, Using daily satellite observations to estimate emissions of short-lived air pollutants on a mesoscopic scale, *J. Geophys. Res.*, 117, 2012, [doi:10.1029/2012JD017817](https://doi.org/10.1029/2012JD017817)

Naus, S., Maasackers, J. D., Gautam, R., Omara, M., Stikker, R., Veenstra, A. K., Nathan, B., Irakulis-Loitxate, I., Guanter, L., Pandey, S., Girard, M., Lorente, A., Borsdorff, T., and Aben, I.: Assessing the Relative Importance of Satellite-Detected Methane Superemitters in Quantifying Total Emissions for Oil and Gas Production Areas in Algeria, *Environ. Sci. Technol.*, 57, 19545–19556, <https://doi.org/10.1021/acs.est.3c04746>, 2023.

Omara, M., Sullivan, M. R., Li, X., Subramanian, R., Robinson, A. L., and Presto, A. A.: Methane Emissions from Conventional and Unconventional Natural Gas Production Sites in the Marcellus Shale Basin, *Environ Sci Technol*, 50, 2099–2107, <https://doi.org/10.1021/acs.est.5b05503>, 2016.

Peng, S., Giron, C., Liu, G., d'Aspremont, A., Benoit, A., Lauvaux, T., Lin, X., De Almeida Rodrigues, H., Saunois, M., and Ciais, P.: High-resolution assessment of coal mining methane emissions by satellite in Shanxi, China, *iScience*, 26, 108375, <https://doi.org/10.1016/j.isci.2023.108375>, 2023.

Peng, S., Piao, S., Bousquet, P., Ciais, P., Li, B., Lin, X., Tao, S., Wang, Z., Zhang, Y., and Zhou, F.: Inventory of anthropogenic methane emissions in mainland China from 1980 to 2010, *Atmos Chem Phys*, 16, 14545–14562, <https://doi.org/10.5194/acp-16-14545-2016>, 2016.

Qu, Z., Jacob, D. J., Shen, L., Lu, X., Zhang, Y., Scarpelli, T. R., Nesser, H., Sulprizio, M. P., Maasackers, J. D., Bloom, A. A., Worden, J. R., Parker, R. J., and Delgado, A. L.: Global distribution of methane emissions: a comparative inverse analysis of observations from the TROPOMI and GOSAT satellite instruments, *Atmos Chem Phys*, 21, 14159–14175, <https://doi.org/10.5194/acp-21-14159-2021>, 2021.

Sadavarte, P., Pandey, S., Maasackers, J. D., Lorente, A., Borsdorff, T., Denier Van Der Gon, H., Houweling, S., and Aben, I.: Methane Emissions from Superemitting Coal Mines in Australia Quantified Using TROPOMI Satellite Observations, *Environ. Sci. Technol.*, 55, 16573–16580, <https://doi.org/10.1021/acs.est.1c03976>, 2021.

Saunois, M., Martinez, A., Poulter, B., Zhang, Z., Raymond, P., Regnier, P., Canadell, J. G., Jackson, R. B., Patra, P. K., Bousquet, P., Ciais, P., Dlugokencky, E. J., Lan, X., Allen, G. H., Bastviken, D., Beerling, D. J., Belikov, D. A., Blake, D. R., Castaldi, S., Crippa, M., Deemer, B. R., Dennison, F., Etiope, G., Gedney, N., Höglund-Isaksson, L., Holgerson, M. A., Hopcroft, P. O., Hugelius, G., Ito, A., Jain, A. K., Janardan, R., Johnson, M. S., Kleinen, T., Krummel, P., Lauerwald, R., Li, T., Liu, X., McDonald, K. C., Melton, J. R., Mühle, J., Müller, J., Murguía-Flores, F., Niwa, Y., Noce, S., Pan, S., Parker, R. J., Peng, C., Ramonet, M., Riley, W. J., Rocher-Ros, G., Rosentretter, J. A., Sasakawa, M., Segers, A., Smith, S. J., Stanley, E. H., Thanwerdas, J., Tian, H., Tsuruta, A., Tubiello, F. N., Weber, T. S., Van Der Werf, G., Worthy, D. E., Xi, Y., Yoshida, Y., Zhang, W., Zheng, B., Zhu, Q., Zhu, Q., and Zhuang, Q.: Global Methane Budget 2000–2020, <https://doi.org/10.5194/essd-2024-115>, 6 June 2024.

Saunois, M., Stavert, A. R., Poulter, B., Bousquet, P., Canadell, J. G., Jackson, R. B., Raymond, P. A., Dlugokencky, E. J., Houweling, S., Patra, P. K., Ciais, P., Arora, V. K., Bastviken, D., Bergamaschi, P., Blake, D. R., Brailsford, G., Bruhwiler, L., Carlson, K. M., Carrol, M., Castaldi, S., Chandra, N., Crevoisier, C., Crill, P. M., Covey, K., Curry, C. L., Etiope, G., Frankenberg, C., Gedney, N., Hegglin, M. I., Höglund-Isaksson, L., Hugelius, G., Ishizawa, M., Ito, A., Janssens-Maenhout, G., Jensen, K. M., Joos, F., Kleinen, T., Krummel, P. B., Langenfelds, R. L., Laruelle, G. G., Liu, L., Machida, T., Maksyutov, S., McDonald, K. C., McNorton, J., Miller, P. A., Melton, J. R., Morino, I., Müller, J., Murguía-Flores, F., Naik, V., Niwa, Y., Noce, S., O'Doherty, S., Parker, R. J., Peng, C., Peng, S., Peters, G. P., Prigent, C., Prinn, R., Ramonet, M., Regnier, P., Riley, W. J., Rosentretter, J. A., Segers, A., Simpson, I. J., Shi, H., Smith, S. J., Steele, L. P., Thornton, B. F., Tian, H., Tohjima, Y., Tubiello, F. N., Tsuruta, A., Viovy, N., Voulgarakis, A., Weber, T. S., van Weele, M., van der Werf, G. R., Weiss, R. F., Worthy, D., Wunch, D., Yin, Y., Yoshida, Y., Zhang, W., Zhang, Z., Zhao, Y., Zheng, B., Zhu, Q., Zhu, Q., and Zhuang, Q.: The Global Methane Budget 2000–2017, *Earth Syst Sci Data*, 12, 1561–1623, <https://doi.org/10.5194/essd-12-1561-2020>, 2020.

Saunois, M., Martinez, A., Poulter, B., Zhang, Z., Raymond, P., Regnier, P., Canadell, J. G., Jackson, R. B., Patra, P. K., Bousquet, P., Ciais, P., Dlugokencky, E. J., Lan, X., Allen, G. H., Bastviken, D., Beerling, D. J., Belikov, D. A., Blake, D. R., Castaldi, S., Crippa, M., Deemer, B. R., Dennison, F., Etiope, G., Gedney, N., Höglund-Isaksson, L., Holgerson, M. A., Hopcroft, P. O., Hugelius, G., Ito, A., Jain, A. K., Janardanan, R., Johnson, M. S., Kleinen, T., Krummel, P., Lauerwald, R., Li, T., Liu, X., McDonald, K. C., Melton, J. R., Mühle, J., Müller, J., Murguía-Flores, F., Niwa, Y., Noce, S., Pan, S., Parker, R. J., Peng, C., Ramonet, M., Riley, W. J., Rocher-Ros, G., Rosentretter, J. A., Sasakawa, M., Segers, A., Smith, S. J., Stanley, E. H., Thanwerdas, J., Tian, H., Tsuruta, A., Tubiello, F. N., Weber, T. S., van der Werf, G., Worthy, D. E., Xi, Y., Yoshida, Y., Zhang, W., Zheng, B., Zhu, Q., Zhu, Q., and Zhuang, Q.: Global Methane Budget 2000–2020, *Earth Syst. Sci. Data Discuss.* [preprint], <https://doi.org/10.5194/essd-2024-115>, in review, 2024.

Scarpelli, T. R., Jacob, D. J., Grossman, S., Lu, X., Qu, Z., Sulprizio, M. P., Zhang, Y., Reuland, F., Gordon, D., and Worden, J. R.: Updated Global Fuel Exploitation Inventory (GFEI) for methane emissions from the oil, gas, and coal sectors: evaluation with inversions of atmospheric methane observations, *Atmos Chem Phys*, 22, 3235–3249, <https://doi.org/10.5194/acp-22-3235-2022>, 2022.

Scarpelli, T. R., Jacob, D. J., Grossman, S., Lu, X., Qu, Z., Sulprizio, M. P., Zhang, Y., Reuland, F., Gordon, D., and Worden, J. R.: Updated Global Fuel Exploitation Inventory (GFEI) for methane emissions from the oil, gas, and coal sectors: evaluation with inversions of atmospheric methane observations, *Atmospheric Chem. Phys.*, 22, 3235–3249, <https://doi.org/10.5194/acp-22-3235-2022>, 2022.

Shen, L., Jacob, D. J., Gautam, R., Omara, M., Scarpelli, T. R., Lorente, A., Zavala-Araiza, D., Lu, X., Chen, Z., and Lin, J.: National quantifications of methane emissions from fuel exploitation using high resolution inversions of satellite observations, *Nat. Commun.*, 14, 4948, <https://doi.org/10.1038/s41467-023-40671-6>, 2023.

Sheng, J., Song, S., Zhang, Y., Prinn, R. G., and Janssens-Maenhout, G.: Bottom-Up Estimates of Coal Mine Methane Emissions in China: A Gridded Inventory, Emission Factors, and Trends, *Environ Sci Technol Lett*, 6, 473–478, <https://doi.org/10.1021/acs.estlett.9b00294>, 2019.

Soulie, A., Granier, C., Darras, S., Zilbermann, N., Doumbia, T., Guevara, M., Jalkanen, J.-P., Keita, S., Lioussé, C., Crippa, M., Guizzardi, D., Hoesly, R., and Smith, S. J.: Global anthropogenic emissions (CAM5-GLOB-ANT) for the Copernicus Atmosphere Monitoring Service simulations of air quality forecasts and reanalyses, *Earth Syst. Sci. Data*, 16, 2261–2279, <https://doi.org/10.5194/essd-16-2261-2024>, 2024.

CAMEO

Tibrewal, K., Ciais, P., Sauniois, M., Martinez, A., Lin, X., Thanwerdas, J., Deng, Z., Chevallier, F., Giron, C., Albergel, C., Tanaka, K., Patra, P., Tsuruta, A., Zheng, B., Belikov, D., Niwa, Y., Janardanan, R., Maksyutov, S., Segers, A., Tzompa-Sosa, Z. A., Bousquet, P., and Sciare, J.: Assessment of methane emissions from oil, gas and coal sectors across inventories and atmospheric inversions, *Commun Earth Environ*, 5, 26, <https://doi.org/10.1038/s43247-023-01190-w>, 2024.

Tibrewal, K., Ciais, P., Sauniois, M., Martinez, A., Lin, X., Thanwerdas, J., Deng, Z., Chevallier, F., Giron, C., Albergel, C., Tanaka, K., Patra, P., Tsuruta, A., Zheng, B., Belikov, D., Niwa, Y., Janardanan, R., Maksyutov, S., Segers, A., Tzompa-Sosa, Z. A., Bousquet, P., and Sciare, J.: Assessment of methane emissions from oil, gas and coal sectors across inventories and atmospheric inversions, *Commun. Earth Environ.*, 5, 26, <https://doi.org/10.1038/s43247-023-01190-w>, 2024.

UNFCCC 2017 China Biannual Update Report (Bonn: United Nations Framework Convention on Climate Change) <https://unfccc.int/BURs>

United States Environmental Protection Agency. Global Non-CO2 Greenhouse Gas Emission Projections & Mitigation Potential: 2015-2050. <https://www.epa.gov/global-mitigation-non-co2-greenhouse-gases/global-non-co2-greenhouse-gas-emission-projections> (2019).

United States Environmental Protection Agency. Inventory of US. Greenhouse Gas Emissions and Sinks: 1990-2020. <https://www.epa.gov/ghgemissions/inventory-us-greenhouse-gas-emissions-and-sinks-1990-2020> (2022).

van der A, R. J., Ding, J., and Eskes, H.: Monitoring European anthropogenic NO_x emissions from space, *Atmos. Chem. Phys.*, 24, 7523–7534, <https://doi.org/10.5194/acp-24-7523-2024>, 2024.

van Geffen, J. H. G. M., Eskes, H. J., Boersma, K. F. and Veefkind, J. P.: TROPOMI ATBD of the total and tropospheric NO₂ data products, Report S5P-KNMI-L2-0005-RP, version 2.4.0, 202207-11, KNMI, De Bilt, The Netherlands, <http://www.tropomi.eu/data-products/nitrogen-dioxide/> (last access: 06 Dec. 2022), 2022

Varon, D. J., Jacob, D. J., Hmiel, B., Gautam, R., Lyon, D. R., Omara, M., Sulprizio, M., Shen, L., Pendergrass, D., Nesser, H., Qu, Z., Barkley, Z. R., Miles, N. L., Richardson, S. J., Davis, K. J., Pandey, S., Lu, X., Lorente, A., Borsdorff, T., Maasackers, J. D., and Aben, I.: Continuous weekly monitoring of methane emissions from the Permian Basin by inversion of TROPOMI satellite observations, *Atmospheric Chem. Phys.*, 23, 7503–7520, <https://doi.org/10.5194/acp-23-7503-2023>, 2023.

Veefkind, J. P., Serrano-Calvo, R., De Gouw, J., Dix, B., Schneising, O., Buchwitz, M., Barré, J., Van Der A, R. J., Liu, M., and Levelt, P. F.: Widespread Frequent Methane Emissions From the Oil and Gas Industry in the Permian Basin, *J. Geophys. Res. Atmospheres*, 128, e2022JD037479, <https://doi.org/10.1029/2022JD037479>, 2023.

Zavala-Araiza, D., Lyon, D. R., Alvarez, R. A., Davis, K. J., Harriss, R., Herndon, S. C., Karion, A., Kort, E. A., Lamb, B. K., Lan, X., Marchese, A. J., Pacala, S. W., Robinson, A. L., Shepson, P. B., Sweeney, C., Talbot, R., Townsend-Small, A., Yacovitch, T. I., Zimmerle, D. J., and Hamburg, S. P.: Reconciling divergent estimates of oil and gas methane emissions, *Proceedings of the National Academy of Sciences*, 112, 15597–15602, <https://doi.org/10.1073/pnas.1522126112>, 2015.

Zhang, Y., Gautam, R., Pandey, S., Omara, M., Maasackers, J. D., Sadavarte, P., Lyon, D., Nesser, H., Sulprizio, M. P., Varon, D. J., Zhang, R., Houweling, S., Zavala-Araiza, D., Alvarez, R. A., Lorente, A., Hamburg, S. P., Aben, I., and Jacob, D. J.: Quantifying methane emissions from the largest oil-producing basin in the United States from space, *Sci. Adv.*, 6, eaaz5120, <https://doi.org/10.1126/sciadv.aaz5120>, 2020.

CAMEO

Zhang, Y., Jacob, D. J., Lu, X., Maasakkers, J. D., Scarpelli, T. R., Sheng, J.-X., Shen, L., Qu, Z., Sulprizio, M. P., Chang, J., Bloom, A. A., Ma, S., Worden, J., Parker, R. J., and Boesch, H.: Attribution of the accelerating increase in atmospheric methane during 2010–2018 by inverse analysis of GOSAT observations, *Atmos Chem Phys*, 21, 3643–3666, <https://doi.org/10.5194/acp-21-3643-2021>, 2021.

Zheng, B., Chevallier, F., Ciais, P., Broquet, G., Wang, Y., Lian, J., and Zhao, Y.: Observing carbon dioxide emissions over China's cities and industrial areas with the Orbiting Carbon Observatory-2, *Atmos. Chem. Phys.*, 20, 8501–8510, [doi:10.5194/acp-20-8501-2020](https://doi.org/10.5194/acp-20-8501-2020), 2020.

Document History

Version	Author(s)	Date	Changes
0.1	P Ciais, K. Tibrewal, Q Shi, J. Ding, R. van der A, N. Boussez	Dec 2024	Initial version
1.0	AS above	Dec 2024	Issued

Internal Review History

Internal Reviewers	Date	Comments
Anne Caroline Lange , FZJ and Jacek Kaminski, IOS-PIB	Dec 2024	

This publication reflects the views only of the author, and the Commission cannot be held responsible for any use which may be made of the information contained therein.